

ORIGINAL ARTICLE

Mutant Profilin1 transgenic mice recapitulate cardinal features of motor neuron disease

Daniel Fil^{1,†}, Abigail DeLoach^{1,†}, Shilpi Yadav², Duah Alkam¹,
Melanie MacNicol³, Awantika Singh⁴, Cesar M. Compadre⁴,
Joseph J. Goellner⁵, Charles A. O'Brien⁵, Tariq Fahmi¹, Alexei G. Basnakian^{1,6},
Noel Y. Calingasan⁷, Jodi L. Klessner⁸, Flint M. Beal⁷, Owen M. Peters⁹,
Jake Metterville⁹, Robert H. Brown, Jr⁹, Karen K.Y. Ling¹⁰, Frank Rigo¹⁰,
P. Hande Ozdinler⁸ and Mahmoud Kiaei^{1,2,11,12,13,*}

¹Department of Pharmacology and Toxicology, ²Physiology and Biophysics, ³Department of Neurobiology and Developmental Sciences, ⁴Department of Pharmaceutical Sciences, ⁵Division of Endocrinology, University of Arkansas for Medical Sciences, AR, USA, ⁶Central Arkansas Veterans Healthcare System, Little Rock, AR 72205, USA, ⁷Feil Family Brain and Mind Research Institute, Weill Cornell Medicine, New York, NY 10065, USA, ⁸Department of Neurology, Northwestern University, Feinberg School of Medicine, 303 E. Chicago Ave, Chicago, IL 60611, USA, ⁹Department of Neurology, University of Massachusetts Medical School, Worcester, MA 01605, USA, ¹⁰Feil Family Brain and Mind Research Institute, Weill Cornell Medicine, New York, NY, 10065, USA, ¹¹Center for Translational Neuroscience, ¹²Department of Neurology and ¹³Department of Geriatrics, The University of Arkansas for Medical Sciences, AR, USA

*To whom correspondence should be addressed at: Tel: +1-5016867936; Fax: +15016865521; Email: mkiaei@uams.edu

Abstract

The recent identification of profilin1 mutations in 25 familial ALS cases has linked altered function of this cytoskeleton-regulating protein to the pathogenesis of motor neuron disease. To investigate the pathological role of mutant profilin1 in motor neuron disease, we generated transgenic lines of mice expressing human profilin1 with a mutation at position 118 (hPFN1^{G118V}). One of the mouse lines expressing high levels of mutant human PFN1 protein in the brain and spinal cord exhibited many key clinical and pathological features consistent with human ALS disease. These include loss of lower (ventral horn) and upper motor neurons (corticospinal motor neurons in layer V), mutant profilin1 aggregation, abnormally ubiquitinated proteins, reduced choline acetyltransferase (ChAT) enzyme expression, fragmented mitochondria, glial cell activation, muscle atrophy, weight loss, and reduced survival. Our investigations of actin dynamics and axonal integrity suggest that mutant PFN1 protein is associated with an abnormally low filamentous/globular (F/G)-actin ratio that may be the underlying

[†]The authors wish it to be known that, in their opinion, the first two authors should be regarded as joint First Authors.

Received: September 5, 2016. Revised: December 8, 2016. Accepted: December 16, 2016

© The Author 2016. Published by Oxford University Press.

This is an Open Access article distributed under the terms of the Creative Commons Attribution Non-Commercial License (<http://creativecommons.org/licenses/by-nc/4.0/>), which permits non-commercial re-use, distribution, and reproduction in any medium, provided the original work is properly cited. For commercial re-use, please contact journals.permissions@oup.com

cause of severe damage to ventral root axons resulting in a Wallerian-like degeneration. These observations indicate that our novel profilin1 mutant mouse line may provide a new ALS model with the opportunity to gain unique perspectives into mechanisms of neurodegeneration that contribute to ALS pathogenesis.

Introduction

Amyotrophic lateral sclerosis (ALS) is a fatal neurodegenerative disease characterized by the loss of upper and lower motor neurons. Affected individuals develop progressive muscle weakness and atrophy, eventually leading to death due to respiratory failure (1,2). Clinical studies and extensive basic research have provided initial insight into the pathogenic mechanisms of selective motor neuron degeneration. Nevertheless, the aetiology of sporadic ALS (sALS) remains largely unknown. Cases of familial ALS (fALS) account for ~20% of ALS patients, and in approximately half of the affected families, fALS has been linked to a growing collection of gene mutations (e.g., *SOD1*, *TARDBP*, *FUS/TLS*, *OPTN*, *UBQLN2*, *VCP*, *hnrRNA2B1*, *hnrNPA1*, *TBK1*, *TUBA4A* and *C9ORF72*) (3–10). The identification of these mutant genes establishes new rationale for exploring specific pathogenic processes and mechanisms as the basis of motor neuron death in ALS. Some of the genes linked to fALS have been used to generate mouse models to mimic ALS, and the most popular mouse models for ALS are the *SOD1*-based mouse models (11–14). Other mouse and rat models generated are *TARDBP*, *FUS*, and *C9ORF72* (15–19). *SOD1* mutant mice are the most consistent model of ALS to date and have been highly informative in increasing our understanding of the role of mutant proteins in ALS and instrumental in therapeutic development. Therefore, additional mouse models of ALS that are equally consistent or better are desperately needed to gain further insights into the disease and discover novel pathways that could be targeted for therapeutic development to cure the disease, or at least slow its progression. We have developed such a model, which is described in this manuscript.

Recent identification of mutations in the profilin1 (*PFN1*) gene in 25 human fALS patients focused attention on cytoskeletal dysfunction as a neurodegenerative factor in ALS. To date, eight different mutations (A20T, C71G, G118V, M114T, E117G, T109M, R136W, Q139L) in the profilin1 protein have been reported in the affected families (20–23). Profilin1 is ubiquitously expressed during all embryonic stages and in nearly all adult cell types and tissues (24). The most recognized function of profilin1 is its ability to regulate the assembly of filamentous actin (F-actin), implicating its involvement in cytoskeletal regulation, cell division, differentiation, migration, and maintenance (25–28). Profilin1 interacts with more than 50 ligands and binding partners involved in multiple cellular processes ranging from gene transcription, growth cone formation, axonal development and maintenance, to membrane trafficking. profilin1 regulates PI(3,4)P(2) (phosphatidylinositols) in MDA-MB-231 cells, and profilin1's interaction with lipid products of PI3 kinase suggests that the plasma membrane may be a site of its action because accumulating evidence links profilin1 to signal transduction via G-proteins (29–32). The actin-binding and actin-independent functions of profilin1, as described above, argue for its importance in the maintenance of neuronal integrity by modulating cytoskeletal dynamics, axonal health, mitochondrial transport, and other cellular functions.

To shed light into possible abnormalities of profilin1 structure and/or function, which is caused by the G118V mutation associated with fALS, we used X-ray crystallography data from bovine profilin1 to construct a structural model for human profilin1. Using the PyMOL computer software program and molecular

visualization system, we were able to depict the location of mutant amino acid residues relative to the actin-binding site (Supplementary Material, Fig. S1A). Given the proximity of the G118V to the actin-binding site and considering the side-chain size difference incurred by substitution of valine for glycine, it is possible that this mutation profoundly impacts profilin1's interaction with G-actin or renders it ineffective in catalyzing the exchange of actin-ADP for actin-ATP (33). A notable effect of the G118V mutation, considering the small side chain of glycine (-H) and large side chain of valine (-CH-(CH₃)₂), may result in the disruption of the secondary structure of profilin1, resulting in unstable protein folding and attenuation of profilin1 interaction with G-actin, its ligands, and other binding partners. It became clear that to understand how changes in the profilin1 protein e.g. glycine to valine residue substitution with a large side-chain difference, other recent human C71G and M114T mutations, and new findings from crystallographic studies (34) it would be necessary to create an animal model expressing mutated profilin1. This would allow us to begin to dissect out the mechanisms by which this mutation causes neurodegeneration *in vivo* and contributes to the pathogenesis of fALS. Accordingly, we generated transgenic mouse lines overexpressing hPFN1^{G118V} and hPFN1^{WT} to investigate the molecular and pathogenic mechanisms of mutant profilin1 toxicity towards understanding the fundamental processes by which profilin1 influences motor neuron function, and to enable discovery of novel, promising therapeutic strategies. The novel mouse model that we have generated exhibits ALS-like pathogenic and behavioural phenotypes, and this is proof of principle that profilin1 mutation cause ALS. Additionally our study provides new information to advance our understanding of mechanisms of mutant profilin1 toxicity. Our new hPFN1^{G118V} mouse offers the opportunity to define specific roles of profilin1 in protein aggregations, neuronal dysfunction, axonal degeneration, actin dynamics, and it allows us to establish the importance of the equilibrium of (G)-actin and (F)-actin that is essential for cell division, adhesion, and motility as well as cytoskeletal remodeling, neuronal development, pathfinding, and synaptic plasticity.

Results

Generation of profilin1 transgenic mice

To assess the effects of mutant profilin1 on motor neuron degeneration *in vivo*, we generated transgenic mice overexpressing untagged mutant human profilin1 (hPFN1^{G118V}) and wild type (WT) human profilin1 (hPFN1^{WT}) using a single transgene vector construct. This vector construct contained hPFN1^{G118V} cDNA placed in front of the mouse prion promoter (*PrP*), which has been previously used for generating transgenic mouse models of neurodegeneration, to drive the transgene expression in the central nervous system (Supplementary Material, Fig. S1A) (15,35,36). Human and mouse profilin1 amino acid (AA) sequences differ by six big residues with significant difference in the side chains (Supplementary Material, Fig. S1B). These residues and G118V accounted for slight differences in gel mobility and partial separation of human and mouse profilin1 bands. A Western blot comparison of profilin1 protein (endogenous mouse and untagged human PFN1) between the spinal cord tissues of highly expressing

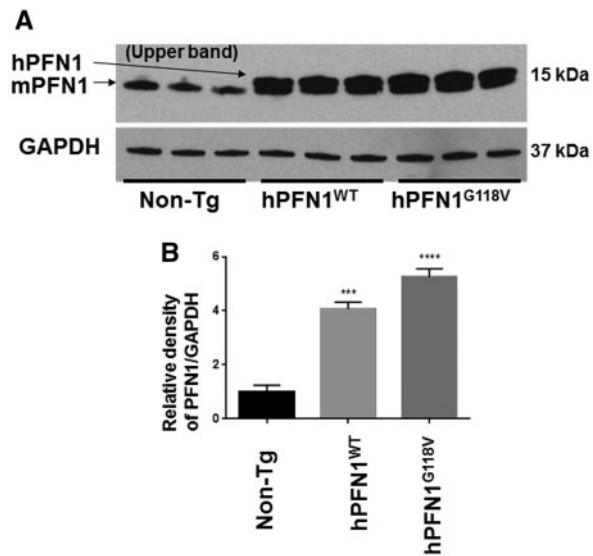


Figure 1. Human and mouse Profilin 1 expression levels. (A) Western blot analysis of mouse profilin 1 (PFN1) and untagged human PFN1 levels probed with anti-PFN1 antibody in 30 μ g samples of total spinal cord homogenates from non-transgenic (non-TG), transgenic hPFN1^{WT}, and transgenic hPFN1^{G118V} lines. hPFN1^{G118V/WT} and mPFN1 migrated closer together and were seen as a doublet. Human PFN1 migrated behind mouse PFN1, as shown by arrows, which was due to 6 different amino acid residues. (B) Quantification of the band relative density (single bands in non-TG mice and double bands in transgenic mice) were normalized to GAPDH and presented as mean \pm SEM. Asterisks denote significantly different PFN1 protein levels in transgenic lines versus non-TG, t-test, with Bonferroni post hoc, *** $P \leq 0.01$, **** $P < 0.0001$. $n = 3$ for each group of mice.

hPFN1^{G118V} mice, hPFN1^{WT} mice, and non-transgenic (non-TG) mice revealed that PFN1 protein levels at 5.25 ± 0.53 (PFN1^{G118V}) and 4.06 ± 0.44 (PFN1^{WT}), and 1.00 ± 0.24 (non-TG) fold relative to the non-TG mouse PFN1 (Fig. 1). Human PFN1 expression under the control of a prion promoter was expressed in the brain, spinal cord, and to a lesser degree in skeletal muscle, while the liver did not express the transgene (Supplementary Material, Fig. S2A). The temporal expression of PFN1 was examined in the spinal cords of mice from P50, P111, P136 and P209 by western blotting. The expression levels of profilin1 in non-TG and hPFN1^{G118V} mice levels didn't change (Supplementary Material, Fig. S2B).

Highly expressing hPFN1^{G118V} transgenic mice exhibited motor-related phenotypes that progressively deteriorated with time. These mice were regularly monitored from birth for signs of motor dysfunction and ALS symptoms (please see Material and Methods section for a detailed description of behavioural assays). There was no obvious difference in the time of disease onset between males and females. Different to other mice, hPFN1^{G118V} mice displayed signs of disease from postnatal day (P) P120 through P130 and rapidly progressed to end-stage disease (see Material and Methods). These symptoms began in the hind limbs, noticed as asymmetrical hind limb display and reflex, fine tremor, and appearance of angle in hind limb at the ankle joint where gastrocnemius and tibialis muscle tendons are attached. These initial subtle signs led to gradual hind limb claspings, further tremor development, and hind limb skeletal muscle weakness. Next, mice developed gait abnormalities and a duck-like walking pattern, spasticity, and an inability to elevate the tail. These symptoms were followed by weight loss and attenuation of muscle strength, as determined by a motor performance test. In the final disease stages, hPFN1^{G118V} mice drag their hind limbs, develop kyphosis, and finally became non-

ambulatory and moribund (Fig. 2). The phenotype and pathological characteristics of these mice are described below. The hPFN1^{WT} mice were followed until P300 and did not reveal any significant differences in gross anatomy, life span, weight, rotarod performance, and stride length, as compared to non-TG animals (Fig. 2), indicating that overexpression of hPFN1^{WT} in mice does not cause any obvious ALS-like phenotype.

Effect of mutant profilin1 on gross morphology and survival

Since voluntary muscle paralysis is a hallmark of human ALS, we sought to determine if the expression of mutant profilin1 is sufficient to cause skeletal muscle atrophy and pathology with a possible impact on motor behaviour. hPFN1^{G118V} transgenic mice exhibited progressively deteriorating motor dysfunction with the onset of symptoms at P120–130 and rapid progression to end-stage disease (P165–210). The symptoms began in the hind limbs as an asymmetrical hind limb reflex, a fine tremor, and the appearance of an angle in the hind limb at the ankle joint, where the gastrocnemius and tibialis muscle tendons are attached (Fig. 3). These initial subtle signs were followed by a gradual decline in locomotion and, at the fully symptomatic stage (P160); the average stride length was reduced to 3.31 ± 1.1 cm (Fig. 2C). In contrast, transgenic hPFN1^{WT} and non-TG mice had comparable stride lengths (6.0 ± 0.5 cm and 6.6 ± 0.9 cm, respectively) that were maintained during locomotion monitoring from P60 up to P300 (Fig. 2C). The stride length in PFN1^{G118V} mice reached 0.00 cm (data not shown) in the final disease stages. These mice developed kyphosis and dragged their hind legs with the help of front limb mobility until the end stage of disease (S.4 and S.5, movies of one hPFN1^{G118V} mouse at the fully symptomatic stage and near the end stage of disease). Ultimately, PFN1^{G118V} mice became non-ambulatory and moribund. Animals in the end stages of disease were considered moribund when they could not right themselves within 20s and sacrificed humanely. The age when sacrificed was counted as the age of death. The weight loss in hPFN1^{G118V} mice started at \sim P150, as shown in Figure 2A. The body weight of hPFN1^{G118V} mice at P203 was reduced to 21.4 ± 6.1 g (hPFN1^{G118V}, $n = 15$) from the initial peak weight of \sim 30 g, while the weight of non-TG and hPFN1^{WT} mice was higher (non-TG, 35.8 ± 9.1 g, $n = 10$; hPFN1^{WT} 33.2 ± 5.4 g, $n = 10$). This weight loss in hPFN1^{G118V} mice was also evident in a marked reduction in hind limb gastrocnemius and tibialis muscle sizes (Fig. 3A and B).

The ability of hPFN1^{G118V} mice to stay on a rotating rod was impaired, as compared to control animals (Fig. 2B). Starting at P140, hPFN1^{G118V} mice demonstrated significantly shorter latency on rotarod that gradually deteriorated and eventually reached zero latency before falling (Fig. 2B). The average age of death for both males and females combined was 202 ± 30 days. The hPFN1^{G118V} females reached the end stage of disease at $P191 \pm 30$ ($n = 26$; range P139 to P271) and males reached the end stage of disease at $P213 \pm 29$ ($n = 43$; range P153 to P283) (Fig. 2D). The Kaplan-Meier analysis of survival data suggested a significant difference in life-span between hPFN1^{G118V} male and female mice using the logrank (Mantel-Cox) test (Chi-Square $+7.102$; P value = 0.0077).

Pathologies of mutant profilin1 mice

Mutant profilin1 causes reduced hind limb CMAP amplitude

To address the decline in motor performance, we assessed the effect of mutated human profilin1 on motor units by measuring compound muscle action potential (CMAP) from the tibialis anterior muscle in the hind limbs of disease end-stage hPFN1^{G118V} mice and non-TG littermates (Fig. 4A).

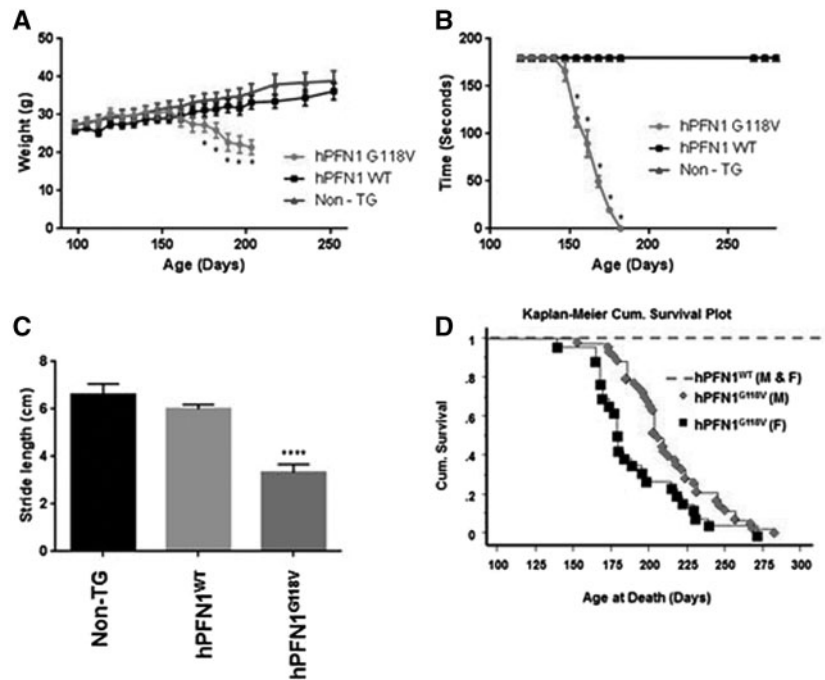


Figure 2. Weight loss, motor performance and survival of hPFN1^{G118V} mice compared to hPFN1^{WT} and non-TG mice. (A) Body weights presented from P100 to P260. The weight of hPFN1^{G118V} mice began to drop from PD 150, $n = 12-15$. A repeated measure ANOVA followed by a Student-Newman-Keuls test, $^*P < 0.05$. (B) Rotarod performance, $n = 15/\text{group}$, $^*P < 0.05$. (C) Stride length measured in centimeters (cm) at P160 shows significant stride shortening in hPFN1^{G118V} mice ($n = 10$), repeated measure of ANOVA followed by Student-Newman-Keuls test $^{****}P < 0.0001$. (D) Kaplan-Meier survival plot of male and female hPFN1^{G118V} mice compared to hPFN1^{WT} ($n = 15$), M = Males ($n = 43$), F = Females ($n = 26$). For A–C, data are presented as mean \pm SEM. Asterisks in A, B, and C denote significant difference in weight, latency in rotarod, and stride length between hPFN1^{G118V} mice and non-TG or hPFN1^{WT} mice. Female mice survival is significantly shorter than males, as assessed with Kaplan-Meier analysis of survival with logrank (Mantel-Cox) test.



Figure 3. Abnormal phenotype of mutant hPFN1^{G118V} mice. Representative images of (A) physical appearance of mutant hPFN1^{G118V} mice from early-symptomatic (P145), fully symptomatic (P165) to endstage disease (average of P202). (B) Hind limb paralysis in hPFN1^{G118V} (left), normal reflex in non-TG littermates (right) at P165; skeletal muscle atrophy was observed in the hind limbs of hPFN1^{G118V} mice (bottom left) compared to non-TG littermates (bottom right) at P165.

The CMAP amplitudes were drastically reduced in hPFN1^{G118V} mice, as compared to age-matched non-TG controls (non-TG, 81.3 ± 2.1 mV versus hPFN1^{G118V} mice, 24.0 ± 5.5 mV) (Fig. 4B), suggesting muscle function deficits that can be in part due to a reduction of innervating fibres and/or severe muscle atrophy. In addition, we observed a prolonged CMAP duration in hPFN1^{G118V} versus controls (non-TG, 2.9 ± 0.2 ms versus hPFN1^{G118V} mice, 3.4 ± 0.2 ms), which are signs of myopathy associated with critical illness (37) (Supplementary Material, Fig. S3).

Mutant profilin1 causes neuromuscular junction and muscle denervation

Following the observation of abnormal CMAP recordings, we investigated neuromuscular junction (NMJ) loss and muscle denervation using β -tubulin, synaptophysin (presynaptic neuronal

markers), and α -bungarotoxin (post-synaptic acetylcholine receptor marker). These pre- and postsynaptic markers allowed us to quantify the percentage of innervated, partially innervated, and denervated gastrocnemius NMJs at presymptomatic (P100), fully symptomatic (P165) and end stages of the disease (P202). The presence of both pre- and postsynaptic markers staining was considered an innervated muscle fibre. The partial presence of both pre- and postsynaptic markers was considered an intermediate level of innervation. The absence of co-localization of any presynaptic markers with α -bungarotoxin was considered a denervation. A higher percentage of denervated gastrocnemius muscles was identified in hPFN1^{G118V} mice, as compared to non-TG littermates (Fig. 5). Intermediate denervation in non-TG animals was assessed at $\sim 30\%$, whereas gastrocnemius muscle sections of hPFN1^{G118V} mice displayed significantly higher intermediate innervation,

culminating in ~55% at end-stage disease (Fig. 5B). Similarly, although denervated muscle fibres were rare in non-TG littermates, this finding increased progressively after symptom onset in hPFN1^{G118V} mice, ultimately reaching ~40% of muscle fibres at the end stage of disease (Fig. 5B). We also examined axons in the sciatic nerves using Toluidine blue staining of semi-thin sections of the sciatic nerve from end-stage hPFN1^{G118V} transgenic and non-TG mice. We found degenerating myelinated axons and glia

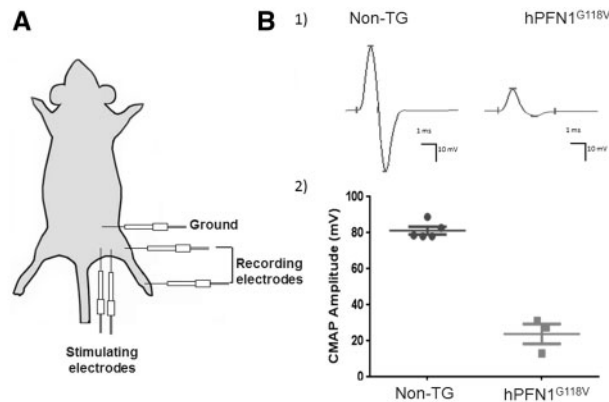


Figure 4. Assessment of compound muscle action potential (CMAP). (A) Electrophysiology system for measuring CMAP from the tibialis anterior muscle in the hind limbs of non-TG and hPFN1^{G118V} mice. (B) Reduction of CMAP in hPFN1^{G118V} mice with end-stage disease at P202. 1) Representative CMAP recordings and 2) CMAP amplitudes recorded from the tibialis anterior muscle. Data represent mean \pm SEM, $n = 4$. Data analysed by t-test.

containing phagocytized myelin in the sciatic nerves of end-stage hPFN1^{G118V} transgenic mice (Fig. 5C). These results suggest that over-expression of mutant hPFN1^{G118V} causes NMJ loss and skeletal muscle fibre denervation, a finding that correlates with disease pathology in ALS patients as well as our observations of impaired motor performance as assessed on a Rotarod machine and measuring the time of latency to drop from rotating rod (Fig. 1B), muscle atrophy (Fig. 2B) and stride length (Fig. 2C).

Mutant profilin1 causes loss of ventral horn spinal neurons

A major characteristic of ALS and possible explanation for the reduced CMAP and NMJ number in tibialis and gastrocnemius muscles of hPFN1^{G118V} mice, respectively, is loss of large ventral horn neurons in the lumbar spinal cord. The ventral horn of the spinal cord houses most of the motor neurons that send their axons to innervate skeletal muscles. To correlate the motor weakness and early death in hPFN1^{G118V} mice with the abundance of spinal ventral horn neurons, we quantified the neurons by an unbiased stereological method of cell counting that combines Nissl stain and a Stereo Investigator computer program (MBF Bioscience, VT, USA). This analysis revealed a significant and progressive loss of ventral horn neurons in the fully symptomatic (beginning from P165) and end stage (P202) of the disease in hPFN1^{G118V} mice (Fig. 6).

Mutant profilin1 is associated with loss of ChAT and mislocalized TDP-43

We also applied immunohistochemistry to spinal cord sections from non-TG and hPFN1^{G118V} mice at the end stage of disease to assess key proteins indicators of the functional status of ventral

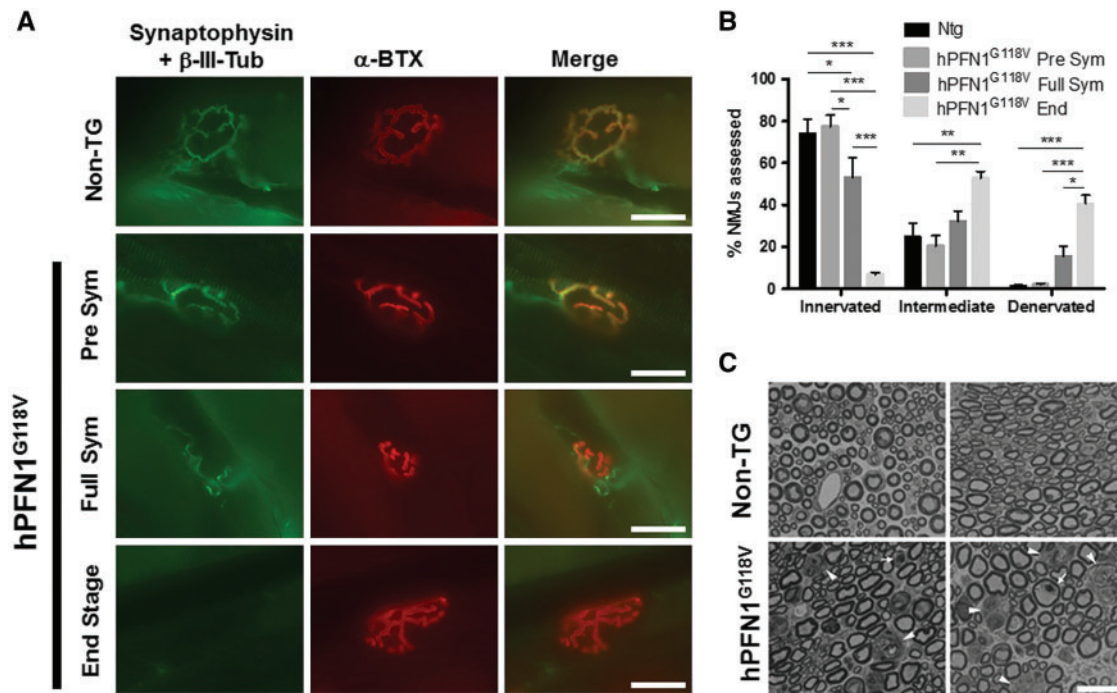


Figure 5. Degeneration of myelinated axons and neuromuscular junctions in symptomatic hPFN1^{G118V} mice. (A) Fluorescent immunostaining of neuromuscular junctions in the gastrocnemius muscles of non-TG (P180) and hPFN1^{G118V} mice at pre-symptomatic (P100), fully symptomatic (P165) and end-stage disease (P202). The red fluorescence is Alexa Fluor 555 conjugated α -bungarotoxin (α -BTX), green fluorescence is combined anti-synaptophysin and anti- β -III-tubulin and merged image shows colocalization of α -BTX and synaptophysin + β -III-tubulin. (B) Percentage of innervated, intermediate innervated or denervated gastrocnemius NMJs assessed per animal (non-TG $n = 5$, total NMJs assessed = 440; hPFN1^{G118V} Pre Sym $n = 4$, total NMJs assessed = 525; hPFN1^{G118V} Full Sym $n = 4$, total NMJs assessed = 537; hPFN1^{G118V} Endstage $n = 3$, total NMJs assessed = 754). Two-way ANOVA with Bonferroni multiple comparisons post-hoc testing was used, * $P < 0.05$, ** $P < 0.01$, *** $P < 0.001$). (C) Toluidine blue staining of semi-thin sections of sciatic nerve from end-stage disease hPFN1^{G118V} transgenic and non-TG mice. Degenerating myelinated axons (arrows) and glia containing phagocytized myelin (arrowheads) were evident in sciatic nerves of end-stage disease hPFN1^{G118V} transgenic mice. Each panel represents a separate animal. Scale bars: A,C = 20 μ m.

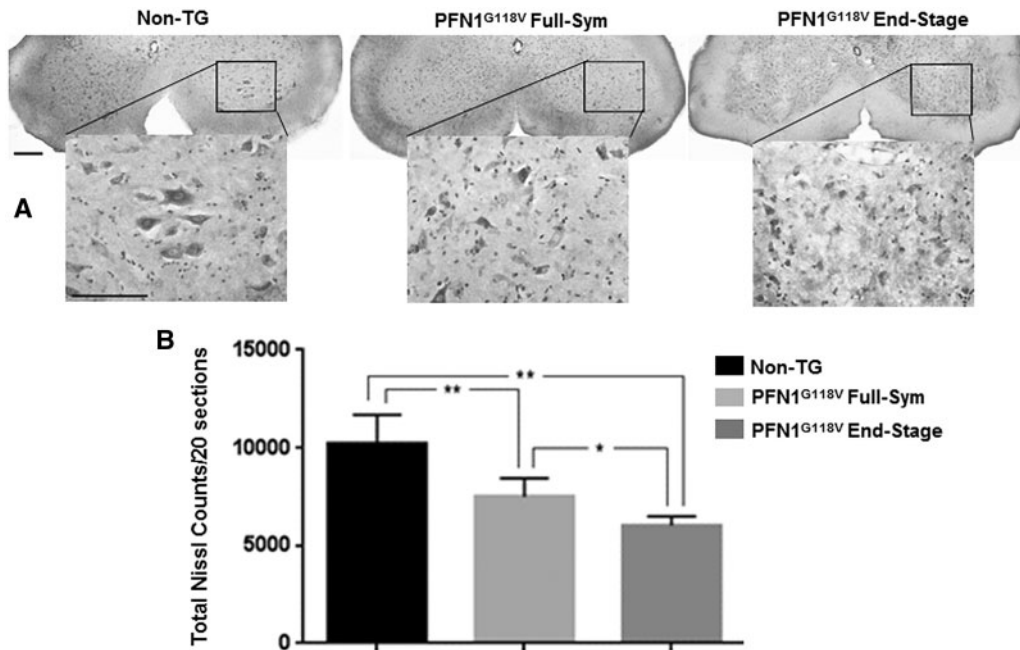


Figure 6. Neuronal cell count in lumbar spinal cord from non-TG and hPFN1^{G118V} mice. (A,B) The effect of hPFN1^{G118V} protein toxicity on lumbar spinal neurons quantified by unbiased stereological count of Nissl stained neurons in spinal cords of hPFN1^{G118V} mice at full symptomatic disease (P165–175) and end-stage disease (P165–210). Nissl-stained count of lumbar spinal cord neurons from similarly aged littermates of control mice is quantified for comparison. High magnification images taken under 40x objective form the black square area of the ventral horn of spinal cord from the 10x objective. Data were analysed by one way ANOVA with Tukey-Kramer post-hoc. Values are mean ± standard deviation with $n = 6$ per group. Scale bar = 100 μ m.

horn neurons (Fig. 7). Haematoxylin and Eosin (H&E) staining revealed dysmorphic looking neurons in the ventral horn of hPFN1^{G118V} mice (Fig. 7A). Initially, we assessed the expression of choline acetyltransferase (ChAT) in motor neurons, the enzyme responsible for the synthesis of the neurotransmitter acetylcholine. Immunostaining showed that ChAT expression was reduced in the spinal cord ventral horn neurons of hPFN1^{G118V} end-stage disease animals, compared to non-TG littermates (Fig. 7B), indicating a likely deficit of acetylcholine neurotransmitter for motor neuron activation. The immunostaining pattern of TDP-43, an RNA editing protein associated with ALS pathology, was more prominent and dense in the neuronal nucleus in the spinal cord ventral horn of hPFN1^{G118V} mice but not in non-TG mice. We also qualitatively detected dense nuclear and punctate cytoplasmic staining with an antibody against TDP-43, in large ventral horn neurons, resembling skein-like type staining, of spinal cord sections from end-stage disease hPFN1^{G118V} mice (Fig. 7C and D). We examined spinal cord sections with an antibody that detects phosphorylated TDP-43 (p409/410 TDP-43) and found a dense nuclear staining, which indicates higher levels of phosphorylated TDP-43 in the nucleus of the spinal cord neurons in hPFN1^{G118V} mice (Fig. 7E and F).

Mutant profilin1 impairs actin polymerization

F/G-actin dynamics in motor neurons is important for cytoskeletal and axonal integrity. It was recently reported that reduced F/G-actin ratio in primary motor neurons and Neuro-2A cells impacts the cytoskeletal pathogenicity and toxicity of mutant profilin1 (22,38). Transiently transfected neurons with a profilin1, C71G or G118V DNA construct found to have shorter dendrites, higher levels of G-actin, and aggregated profilin1 (22). F/G-actin ratio has to be tightly regulated; otherwise, neuronal functions depending on F-actin will be impaired. To assess the

effect of hPFN1^{G118V} on actin dynamics, we examined the F/G-actin ratio in lumbar spinal cord sections from hPFN1^{G118V} mice at presymptomatic, fully symptomatic and end-stage disease and compared these with hPFN1^{WT} and non-TG controls. Sections were stained with phalloidin (labels F-actin) and DNase I (labels G-actin). Signal intensity analysis indicated that the F/G-actin ratio was reduced in the hPFN1^{G118V} mouse spinal cord lumbar sections, as compared with hPFN1^{WT} and non-TG controls (Fig. 8). At the presymptomatic disease stage, the F/G-actin ratio was slightly lower in the hPFN1^{G118V} spinal cord sections, but did not reach a significant difference to control mice; however the ratio in the hPFN1^{G118V} fully symptomatic and the end-stage sections was significantly lower than controls. The F/G-actin ratio in the spinal cord sections of non-TG or hPFN1^{WT} weren't significantly different (Fig. 8). This is our first *in vivo* finding of abnormal F/G-actin ratio, suggesting that mutant profilin1 may be associated with dysregulation of actin polymerization *in vivo*.

Mutant profilin1 and glial activation

In addition to motor neuron pathology and degeneration, we found that mutant profilin1 expression causes glial cell activation. An increase in the expression profile of marker proteins for astrocytes and microglia is typically a sign of their activation and inflammatory reaction. We found notable increases of fluorescently labelled astrocytes and glial cells in the lumbar spinal cord regions of end-stage disease hPFN1^{G118V} mice, as compared to hPFN1^{WT} and non-TG controls, using antibodies for astrocytes and microglial marker proteins (GFAP and Iba1, respectively) (Fig. 9). Finding astrocytosis, microgliosis and neuronal pathologies in hPFN1^{G118V} mice (Figs 6 and 7) suggest that mutant profilin1 toxicity may impact non-neuronal cell types and may not be limited to motor neurons, suggesting a non-cell

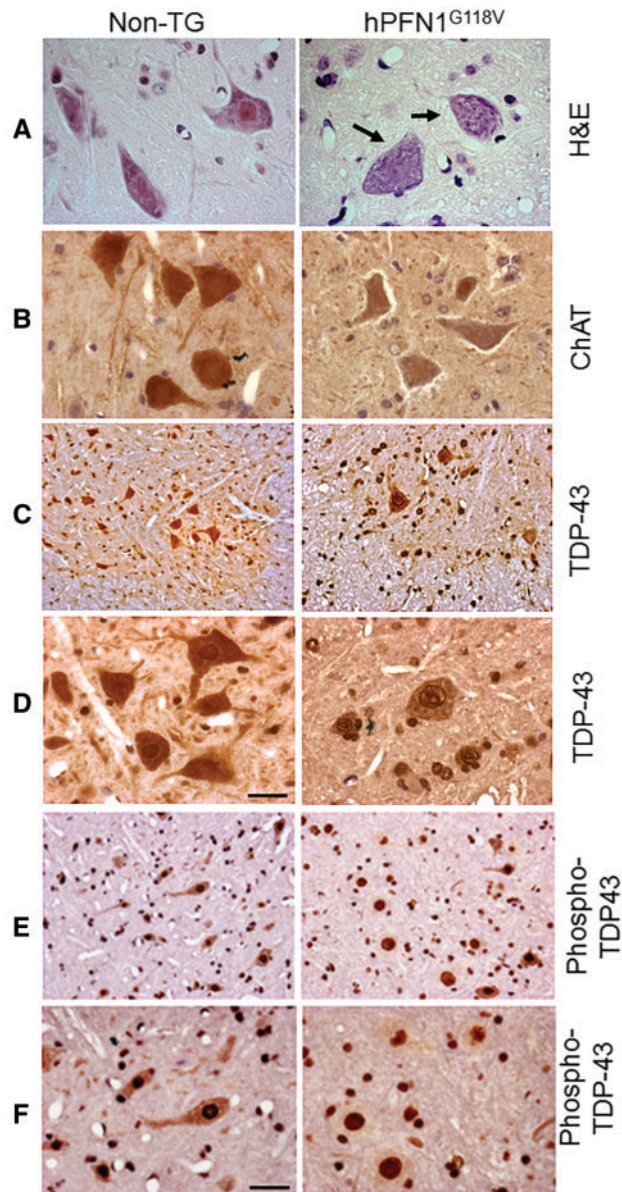


Figure 7. Immunohistochemical analysis of lumbar spinal cord ventral horn. (A) Spinal cord isolated from end-stage diseased mice (P165–210) were processed and stained for pathological abnormalities. H&E stained sections show dysmorphic ventral horn neurons (arrows) in hPFN1^{G118V} mice. (B) Micrograph of sections showing ChAT stained sections from hPFN1^{G118V} spinal cord and light staining for ChAT in the remaining neurons. (C) Spinal cord sections show abnormal TDP-43 staining in spinal ventral horn neurons from hPFN1^{G118V} mice during end-stage disease. (D) Micrograph of sections (high magnitude) stained with anti-TDP-43 showing abnormal TDP-43 staining in spinal ventral horn neurons from end-stage disease hPFN1^{G118V} mice. (E and F) Micrograph of phospho-TDP-43 staining (low & high magnitude) in the ventral horn neurons from end-stage disease hPFN1 mice. Left panels are sections from non-TG littermates, $n = 3$. Scale bars: A, B, D, F, 10 μm ; C, E, 40 μm .

autonomous pathogenic mechanism in the profilin1 mutant mouse model.

Mutant profilin1 aggregation and excess protein ubiquitination

To determine whether mutated profilin1 proteins aggregate, spinal cord homogenates from fully symptomatic/end-stage disease and age-matched hPFN1^{WT} and non-TG control mice

were processed into soluble and insoluble fractions. The analysis of immunoblots revealed that only insoluble fractions from hPFN1^{G118V} mice contained a specific band, recognized with an anti-profilin1 antibody, which was absent in the insoluble fractions obtained from non-TG and hPFN1^{WT} mice (Fig. 10A). The density of bands were quantified and presented as folds over mouse profilin1 in non-TG control (Fig. 10C). We show by immunoblotting that the aggregation of mutant human profilin1 starts as early as P50 and there is a trend for increase of profilin1 aggregation in the spinal cord by age (Fig. 10D). We also probed for ubiquitinated proteins, which commonly are observed in inclusion bodies in multiple neurodegenerative disorders, including ALS. Western blotting of the soluble and insoluble fractions from the spinal cords of hPFN1^{G118V} mice revealed a heavy ubiquitin signal, compared to hPFN1^{WT} and non-TG controls (Fig. 10B), indicative of accumulation of ubiquitinated proteins marked to be processed by the proteasome degradation system. This type of protein modification is a profound resemblance to pathology in spinal cords of human ALS patients, suggesting a similar pathogenic mechanism might be at play in the hPFN1^{G118V} mouse.

Mutant profilin1 causes axonal degeneration and abnormal fragmentation of mitochondrial outer membrane

To gain further insight into the effects of hPFN1^{G118V} expression on motor neuron ventral root axons, we utilized electron microscopy (EM) to visualize axons and organelles at the ultrastructural level. EM images from transversely sectioned ventral roots isolated from L1 to L5 spinal vertebrae demonstrated degenerative axons and aberrant mitochondria with fragmented outer membranes and irregular cristae in the hPFN1^{G118V} mice, as compared to non-TG controls. Irregularly shaped, non-circular, shrunken, and collapsed axons were abundant in the lumbar ventral roots of hPFN1^{G118V} mice. This observed pathology resembles Wallerian-like degeneration, denoted by separation and vacuolization of the myelin sheath and shrinkage of axoplasm (Fig. 11), a pathology observed in ALS patients and other neurodegenerative diseases (reviewed in (39)).

Mutant profilin1 causes upper motor neuron pathology

In addition to lower motor neuron pathology, we determined whether mutant profilin1 expression causes degeneration of upper motor neurons. To this end, we first assessed the overall morphology of the brain. Nissl staining did not reveal any gross morphological abnormalities in the cerebral cortex of hPFN1^{G118V} mice. The ventricles and different brain regions, including the motor cortex, were comparable between non-TG and hPFN1^{G118V} mice (Fig. 12A and B). We used molecular markers that are selectively expressed in the large corticospinal motor neurons (CSMN), located in layer V of the motor cortex, such as CTIP2 (Fig. 12C and D) and Cry-mu (Fig. 12E and F). Higher magnification of Cry-mu expressing CSMN revealed reduced CSMN numbers (Fig. 12E and F). Although CSMN numbers were comparable between non-TG (WT) and hPFN1^{G118V} mice at mid-stage (P150) (non-TG: 79 ± 4 CSMN, $n = 3$ mice, $n = 710$ total neurons counted; hPFN1^{G118V}: 87 ± 3 CSMN, $n = 3$ mice, $n = 780$ total neurons counted), as assessed by the number of CTIP2⁺ neurons in layer V of the motor cortex, there was a significant reduction of CSMN at end-stage (P202) (non-TG: 77 ± 4 CSMN, $n = 6$ mice, $n = 1380$ total neurons counted; hPFN1^{G118V}: 44 ± 3 CSMN, $n = 6$ mice, $n = 792$ neurons counted). CSMN numbers were significantly reduced in hPFN1^{G118V} mice, especially during the end stage of disease, but this was not due

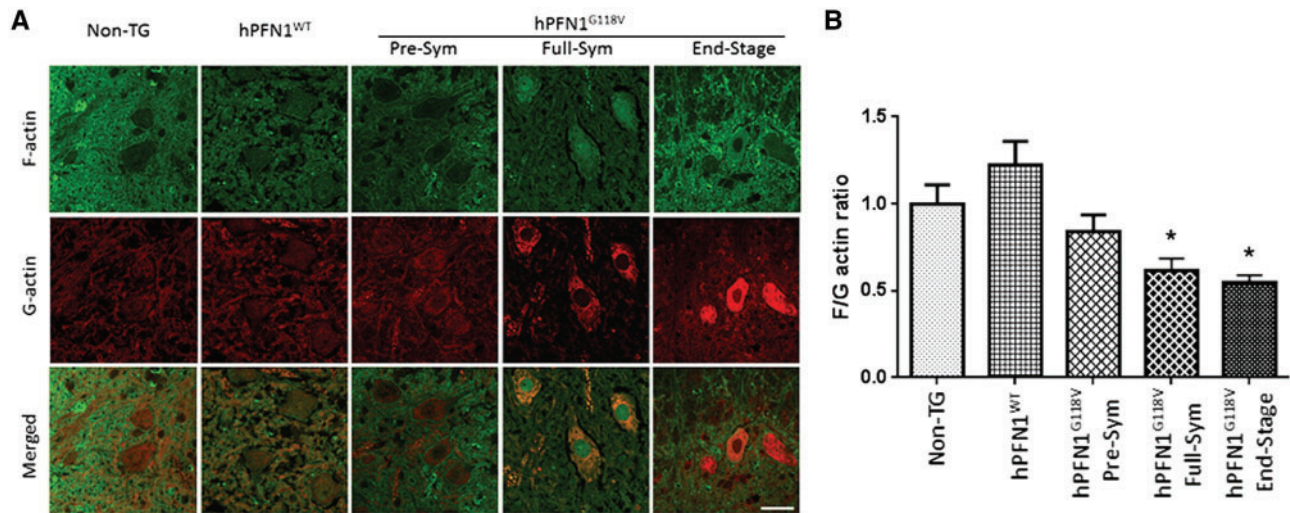


Figure 8. Actin dynamics in non-TG, hPFN1^{WT} and hPFN1^{G118V} mice. Lumbar spinal cord sections were processed to assess G-actin and F-actin status. Representative images show (A) Phalloidin stain (green) F-actin and DNase I stain (red) G-actin in ventral horn neurons of non-TG, hPFN1^{WT}, and hPFN1^{G118V} mice at presymptomatic, fully symptomatic and end-stage disease, $n=9$. (B) Quantification of phalloidin and DNase I signal density plotted as F/G-actin ratio. Values are mean \pm SEM. Data analysed by t-test followed by two-way ANOVA Bonferroni. * $P < 0.05$ relative to non-TG animals, $n=3$, and 3-5 sections were examined per animal. Scale bar = 20 μ m.

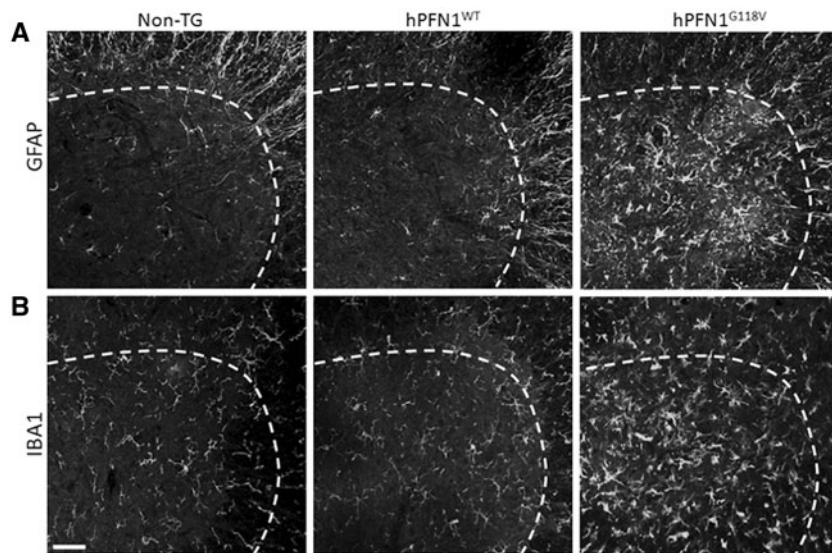


Figure 9. Glial cell activation in spinal cord ventral horn. Lumbar spinal cord sections were examined for glial activation and immunostained with (A) an astrocyte marker (GFAP) and (B) microglia marker (IBA1), which revealed activation of glial cells in the spinal cords of end-stage disease hPFN1^{G118V}, as compared to hPFN1^{WT} and non-TG mice (P175-P205), $n=3$. Scale bar = 50 μ m.

to aging, as the numbers of CSMN in non-TG mice at two different ages were comparable (Fig. 12G).

Apical dendrite degeneration in CSMN can become diseased from different underlying causes (i.e., mSOD1^{G93A}, lack of Alsin function) (40–42), suggesting that apical dendrite degeneration could be a common cellular pathology observed in diseased CSMN. Therefore, we investigated whether apical dendrites of CSMN retain their integrity or instead fail to maintain their cyto-architecture, especially at the apical dendrite. Map2 immunocytochemistry coupled with CTIP2 expression helped identify CSMN and visualize their apical dendrites. Non-TG CSMN had long, prominent apical dendrites that did not include any vacuoles. In striking contrast, CSMN in hPFN1^{G118V} mice had multiple abnormalities in their apical dendrites. In most cases, the apical dendrites were filled with vacuoles, which varied by size

and number (Fig. 12H and I). Interestingly, these abnormalities were present only in the CSMN of hPFN1^{G118V} mice, suggesting the presence of a cellular pathology that is especially observed in CSMN in the presence of mutant profilin1.

Discussion

The present study reports a novel *in vivo* mouse model for ALS overexpressing hPFN1^{G118V} without a tag from a single transgene DNA construct that exhibits behaviours and pathologies closely resembling ALS. Since there is a biochemical evidence that adding a tag on a relatively small profilin1 protein may influence its biochemical binding properties (43), we developed a mouse model that can uniquely model the disease by expressing human mutant profilin1 unmodified. The ALS field has a

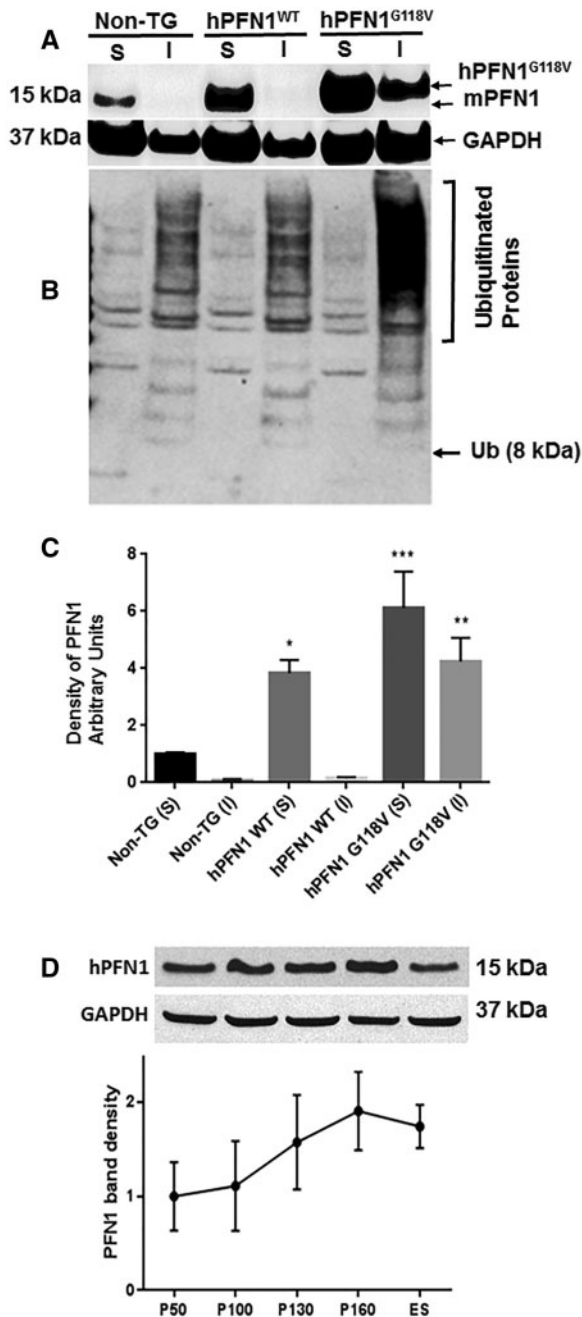


Figure 10. Mutant PFN1^{G118V} aggregation and abnormal protein ubiquitination. Western blot analysis of spinal cords from non-TG, hPFN1^{WT} and hPFN1^{G118V} animals. (A) Profilin 1 signal in soluble (S) and insoluble (I) fractions. An antibody against profilin1 recognizes both mouse and human PFN1. The same blot was probed with anti-GAPDH. (B) Ubiquitinated proteins in soluble (S) and insoluble (I) fractions show a dense smear of protein larger than 50 kDa. (C) Quantification of PFN1 band intensity relative to GAPDH presented as mean \pm SEM. (D) Western blot analysis and quantifications of band density of insoluble fractions from the spinal cord of hPFN1^{G118V} mice from P50 to end-stage disease, $n = 3$ per time point. The increasing trend did not reach statistical significance. This blot was probed with anti-GAPDH for loading control and quantification. Data analysed by *t*-test followed by two-way ANOVA Bonferroni. * $P < 0.05$, ** $P < 0.01$, *** $P < 0.001$ relative to non-TG (S) or (I) respectively. (PD 175-PD 205), $n = 3$ per genotype.

limited number of reliable disease models available to researchers, and this underscores the importance of introducing and validating new mouse models. Our study led to the development and detailed characterization of a transgenic mouse

model for ALS and investigated the effects of mutant profilin1 *in vivo*. We report our findings of neurotoxic mutant profilin1 and describe this novel ALS mouse model as a 'new window' of opportunity for understanding the effects of mutant profilin1 in ALS. As we demonstrated with evidence throughout this manuscript, we found that the expression of hPFN1^{G118V} in mice produces ALS-like symptoms, including loss of lower and upper motor neurons, mutant profilin1 aggregation, abnormally higher levels of ubiquitinated proteins, glial cell activation, muscle atrophy, weight loss and early death. The hPFN1^{G118V} phenotype and pathology closely resembles the phenotype and pathology of human ALS and aligns with other well-characterized transgenic ALS mouse models, for example SOD1 mutants, suggesting shared pathological mechanisms, despite different initial causative factors (11,12,15).

A reduction of ChAT, an important marker for cholinergic neurons, in the ventral horn area of the lumbar spinal cord in hPFN1^{G118V} mice is consistent with a previous report of decreased ChAT activity in spinal cord motor neurons from human ALS patients (44–46). ChAT immunoreactivity reduction indicates the health status of motor neurons in the hPFN1^{G118V} mouse spinal cord. In this study, we show that existing neurons are unable to express high levels of ChAT, compared to wild type controls.

Our analysis of ultrastructural images from ventral root axons by EM shows multiple cellular abnormalities. These include fragmented mitochondria with membrane blebbing and disorganized cristae, cytoskeletal abnormalities, separation and vacuolization of the myelin sheath. These pathological findings resemble Wallerian-like degeneration that occurs in many neurodegenerative diseases, especially those in which axonal transport is impaired (47). The degeneration may reflect the failure of the cytoskeletal infrastructure in dendrites, axons and axonal roots caused by a reduction in the F/G-actin ratio. These pathologies also are consistent with delivering insufficient quantities of essential axonal proteins, like nicotinamide nucleotide adenylyltransferase 2 (NMNAT2), a key initiating event for Wallerian-like degeneration (48). Other studies have indicated that ALS is a distal axonopathy (reviewed in (49)), although it remains unclear whether the distal denervation is primary or secondary to progressive pathology in the motor neuron cell body.

In this study, we found significant neuromuscular junction disruption and denervation of gastrocnemius muscle at the fully symptomatic and end stages of disease. A recent study in which primary mouse hippocampal neurons were transiently transfected with mutant PFN1^{C71G} reported an increase in dendritic arborization and spines, and cytoplasmic inclusions were also found in the neurons (50). However, given the way mutant PFN1^{C71G} impairs profilin1 binding to actin, it is not clear how PFN1^{C71G} transient overexpression stimulation increase dendritic arborization and spines since these same neurons are thought to be burdened with inclusions. Further studies are needed to unravel the effects of mutant profilin1 on cytoskeleton and neuronal processes and determine whether distal axonopathy is the earliest event in PFN1^{G118V} mice.

Other mutations in profilin1 (e.g., C71G, M114T) provide experimental evidence to link the pathogenesis of ALS to cytoskeletal defects (10,22), implying that impaired binding of profilin1 to actin may be an important factor for mutant profilin1 neurotoxicity in ALS. Our finding of a reduced F/G-actin ratio in lumbar spinal cord sections of end-stage disease hPFN1^{G118V} animals strengthens this hypothesis. The T109M and Q139L mutations cause ALS despite unaltered actin binding properties. These mutations are located on the PLP domain (51), which may

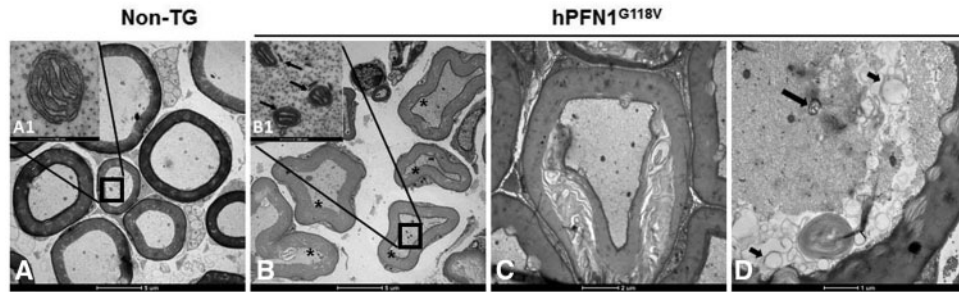


Figure 11. Electron micrographs of ventral root motor axons from hPFN1^{G118V} and non-TG controls. Ultrastructure of lumbar spinal cord, ventral root axons (VR) from non-TG and end-stage hPFN1^{G118V} animals were examined by electron microscopy. (A) Non-TG VR reveals normal axons and normal mitochondria (inset A1). (B) hPFN1^{G118V} VR shows distorted axons containing fragmented mitochondria (inset B1); membrane blebbing and disorganized cristae are also seen. Asterisks mark clapsed, shrunk and degenerating axons. (C) hPFN1^{G118V} VR axon at higher magnification demonstrates separation and vacuolization of damaged myelin sheath and clapping axoplasm. (D) hPFN1^{G118V} VR axon shows vacuoles (short arrows) and the remainder of the damaged mitochondria (long arrow). Representative image of $n = 4$. Scale bars A, B = 5 μm ; C = 2 μm ; D = 1 μm , A1 = 200 nm, B1 = 100 nm.

impact other profilin1 functions. This is an indication for diverse mechanism of profilin1 toxicity, which is discussed in details in our recent review (52). Other functions of profilin1, independent of actin binding, also may be critical to the survival of motor neurons and may contribute to the pathogenicity of ALS. It is plausible that mutations in profilin1 may block the interaction of profilin1 with its ligands and binding partners (i.e., SMN, huntingtin, valosin-containing protein (VCP), Ezrin, and N-WASP) and may affect other important signaling events in the motor neuron (28,53–55).

Actin polymerization is essential for the formation and remodeling of the cytoskeleton and outgrowth of axons and dendrites. Actin polymerization is also important for cell motility, actin attachment to microtubules, and anterograde and retrograde transport of mitochondria into axons and dendrites. Profilin1 activity is particularly important for neurons because of its association with a variety of ligands that are necessary for the integrity of postsynaptic scaffolding, dendritic spine morphology, growth cone formation, axon guidance, neurite outgrowth, clustering of receptors, membrane trafficking, and endocytosis (28). Studies in primary motor neurons found pathological evidence that further links mutant profilin1 alterations to ALS pathogenesis, strengthening the rationale for the involvement of a cytoskeletal component in axonal degeneration (22).

Since profilin1 is evolutionarily highly conserved (Supplementary Material, Fig. S1B), its structural integrity must be vital for its biological functions. As illuminated by a PyMOL-generated model constructed from bovine profilin1 X-ray crystal structure data, the G118V mutation in profilin1 is proximal to the actin-binding site (Supplementary Material, Fig. S1A) and may alter the secondary structure of profilin1 due to side chain difference and impacting the folding and stability of the protein. The aberrant conformation of the binding site alters profilin1–actin interactions with actin and other binding partners. This may have a direct effect on profilin1 stability, solubility, and formation of inclusion bodies or alterations of cytoskeletal dynamics that consequently lead to pathology. A recent study by Bosco and colleagues (34) showed that ALS-linked mutations severely destabilize the native conformation of profilin1 *in vitro* and cause accelerated turnover of the profilin1 protein in cells. Thermochemical analyses of the profilin1 variants C71G, M114T, and G118V suggest a severe effect on tertiary conformation and that PFN1^{C71G} and PFN1^{M114T}, but not PFN1^{E117G}, are destabilized as compared to PFN1^{WT} (34). The observation that

most ALS-linked profilin1 variants are highly prone to aggregation in cultured mammalian cells suggests that the disease-causing mutations induce an abnormal protein conformation (22). Our study and other independent research teams provide support for the concept that profilin1 mutations contribute to ALS pathogenesis by diverse mechanisms (51,56–58). New evidence for the mechanism of profilin1 toxicity that involve the PLP binding domain as well as the actin-binding domain is gaining support. Although, the mutations in the PLP domain of profilin1 (T109M, R136W, Q139L) suggest a more global effect on profilin1 and the toxicity may be caused by actin-binding and other domains, hence actin dynamics and cytoskeletal dysfunction are parts of a bigger picture of neuronal dysfunction (51,58).

Since TAR DNA-binding protein 43 (TDP-43) is a major component in aggregates of ubiquitinated proteins in most types of ALS (8,59,60), it is intriguing that the G118V mutation produced profilin1 aggregation and sequestering of endogenous TDP-43 (38). Co-aggregation of mutant profilin1 with TDP-43 may result in a gain-of-toxic-function of profilin1 mutants. Our results give evidence towards this. We found that TDP-43 abnormally stained in the spinal cord sections of hPFN1^{G118V} mice (Fig. 7C and D) and that immunostaining show that phosphorylated TDP-43 was increased in the nucleus of neurons in the spinal cord of hPFN1^{G118V} mice (Fig. 7E and F).

Exploration of the profilin1 transgenic mouse model in relation to other ALS models provides an extraordinary opportunity to gain insight into the mechanisms of motor neuron degeneration and shed light on shared pathways of disease pathogenesis, despite different causative factors. This new tool in ALS research invites further investigation of profilin1 toxicity, and it can serve as a novel platform to explore cytoskeletal and axonal dysfunctions in ALS and to validate screening of new therapeutics for human ALS.

While our manuscript report of this study was under review, a manuscript was published describing the generation and characterization of another transgenic profilin1 mouse model that expresses V5-PFN1^{C71G} and develops ALS-like symptoms (61). This report is interesting and is significant for the proof of concept that a mutation in profilin1 is one of the main contributors to ALS. A new milestone in ALS research has been reached in that two independent laboratories demonstrate that a profilin1 mutation is a cause for ALS by G118V and C71G in the profilin1 protein. The transgenic profilin1 mice, reported by Yang et al., 2016, developed robust ALS-like symptoms and pathologies, but multiple transgenes were needed to express high levels

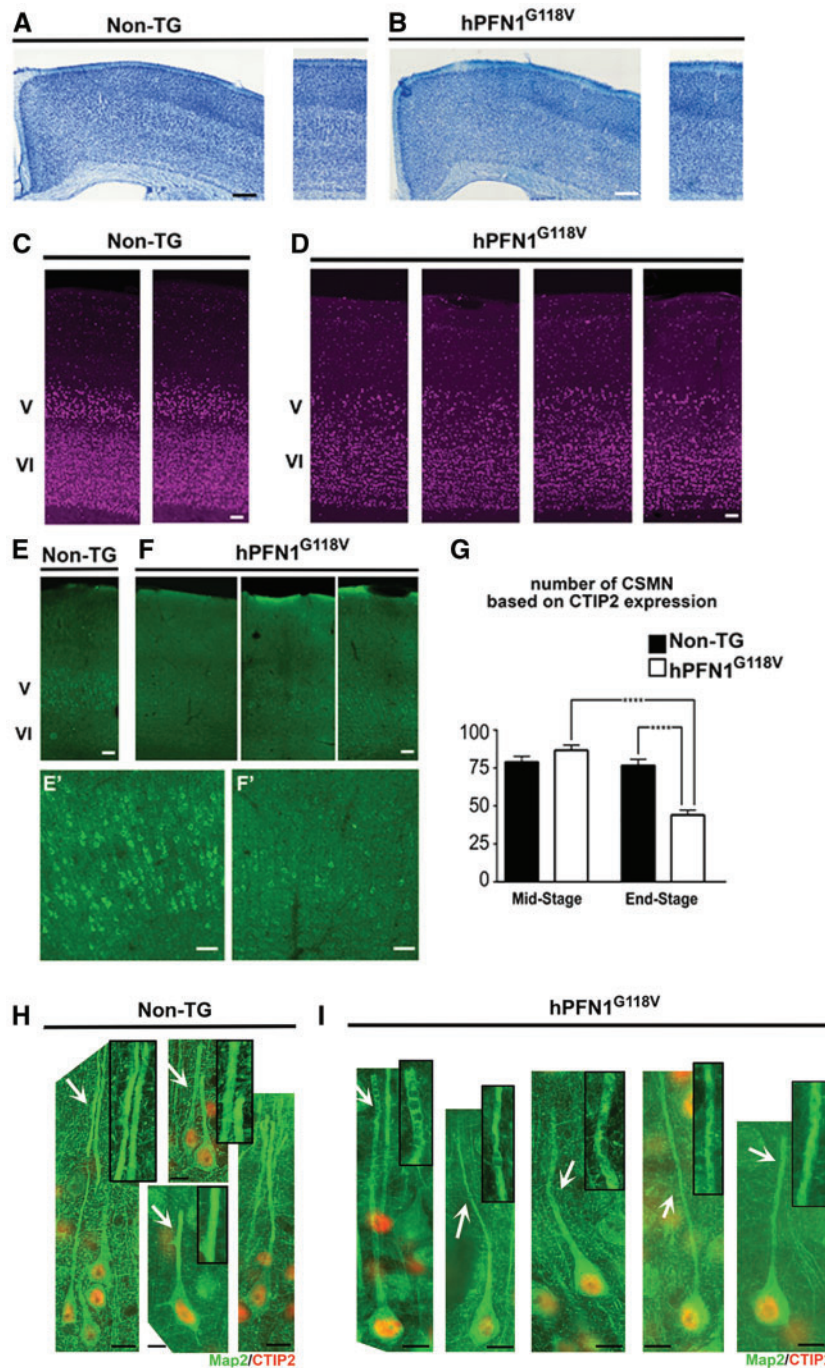


Figure 12. CSMN undergo cellular degeneration in hPFN1^{G118V} mice. (A) Non-TG mice. (B) hPFN1^{G118V} mice. The cerebral cortex appears normal with Nissl staining. The thickness of the motor cortex, size of the ventricles and the cortical layers are comparable, without any signs of massive cortical degeneration. (C,D) High levels of CTIP2 expression marks large pyramidal CSMN in layer V of the motor cortex of both non-TG and hPFN1^{G118V} mice (C), albeit with a potential for reduction in hPFN1^{G118V} mice, as observed in four independent samples. (E,F) Cry-mu, another cellular marker for CSMN, also displays a differential expression pattern in non-TG (E) versus hPFN1^{G118V} mice (F). The reduction in Cry-mu expression of CSMN is more evident in higher magnification (E'-F'). (G) Quantitative assessment of CSMN numbers, based on CTIP2 expression, reveal significant neuron loss, especially during end-stage disease. Bar graph represents the average number of CSMN per 10× objective field in layer V of the motor cortex of non-TG and hPFN1^{G118V} mice during mid-stage disease ($n = 3$ mice for both genotype) and end-stage disease ($n = 6$ mice for both genotype). Bar graphs represent mean \pm SEM. Data analysed with a one-way ANOVA with post hoc Tukey's multiple comparison tests. **** $P < 0.0001$. Scale bars: A, B = 200 μ m; C, D = 100 μ m; E, F = 150 μ m. (H,I) Vacuolization of apical dendrites of diseased CSMN. CTIP2 coupled with Map2 immunocytochemistry reveals profound defects in the apical dendrites of diseased CSMN (H) Four different representative images of non-TG CSMN with healthy apical dendrites. Arrows indicate apical dendrites, which are enlarged to the side. (I) Four different representative images of CSMN in hPFN1^{G118V} mice during end-stage disease. Even though cell bodies are comparable to the non-TG CSMN, the apical dendrites include many vacuoles that are only seen in the brain motor cortex of hPFN1^{G118V} mice. Arrows indicate the site of apical dendrites with profound defects, which are enlarged to the side. Scale bar = 20 μ m.

of mutant profilin1 protein to reduce ALS age of onset because the single transgene mice (Thy1.2-PFN1^{C71G}) had an onset of weakness at ~350 days. Two Prp-PFN1^{C71G} lines did not develop any ALS phenotypes up to P700. Authors crossed the Thy1.2-PFN1^{C71G} littermates to double the transgene and developed homozygote mice in an effort to further increase transgene expression. These double transgenic Thy1-PFN1^{C71G} mice were further crossed with a Prp-PFN1^{C71G} line to create a new triple transgenic line that enabled higher expression levels of mutant profilin1 from multiple loci. The age of disease onset was at ~P140 with paralysis at ~P211, on average. This mouse model could serve as a tool to investigate profilin1 with C71G mutation and neurotoxicity in ALS.

The mouse model that we developed in our laboratory and described herein expresses a high level of mutant profilin1 from a single DNA construct transgene and develop motor weakness at P130–140 and succumb to death because of ALS at P202, on average. This long symptomatic period will enable ALS researchers to utilize this new mouse model to address the neurotoxicity, proteinopathy, cytoskeletal defects and axonal degeneration caused by profilin1 with a G118V mutation. This model is valuable for mechanistic studies and development of therapeutic strategies and can be paired with existing and future ALS mouse models. This is due to the fact that the neurodegeneration and ALS-like symptoms and pathologies are induced by single transgene DNA vector expressing human profilin1 without any tag.

Since cytoskeletal defects in the brain, and spinal cord tissues emerge as one the most important causes of motor neuron vulnerability and progressive degeneration in ALS, here we offer a novel mouse model that can be used to not only study the details of the cytoskeletal defects, cellular mechanisms affected and the underlying causes of the pathology but also for translational studies in the near future.

Materials and Methods

Development of mouse model for ALS

Animals were housed in the animal quarters under 12-hour light/dark conditions and fed 4–5 gram chow diet (Harlan/Teklad #7001) per day per mouse with free access to water. All experimental procedures were conducted in accordance with the Institutional Animal Care and Use Committee (IACUC) guidelines of the University of Arkansas for Medical Sciences (UAMS).

Generation of transgenic hPFN1^{G118V} and hPFN1^{WT} mice

Constructs expressing either wild type (hPFN1^{WT}) or mutant (hPFN1^{G118V}) untagged human profilin1 (Supplementary Material, Fig. S1) were obtained from (NorClone, London, Ontario, Canada). cDNAs were inserted downstream of the mouse prion promoter (moPrP) to achieve robust CNS-specific expression of the single transgene (62) because this promoter has been widely used to model neurodegenerative diseases and ALS (15,36,63). The human wild type and mutant profilin1 cDNA sequences are available upon request. Transgenic mice were produced by pronuclear injection of C57BL/6 fertilized eggs at the UAMS Transgenic Mouse Core facility. All transgenic development procedures were reviewed and approved by the UAMS IACUC and the Central Arkansas Veterans Healthcare System. Mice were genotyped for the presence of the transgene and founders were closely monitored for manifestation of ALS-like

symptoms. Males and females were used at equal ratios, where it was possible. To prevent the tendency to become overweight, mice were fed 4–5 grams of regular chow per mouse, per day with the approval of UAMS IACUC.

Genotyping

Mouse genomic DNA was isolated from ~3 mm tail biopsies with Maxwell 16 mouse tail DNA purification kit (Catalog # AS1120, Promega, Madison, WI) and used as a template for genotyping. PCR was performed using the following steps: 94°C 5 min, (94°C 30 s, 56°C 30 s, 72°C 1 min)×35, 72°C 3 min, and hold 4°C until stopped. Once the genotyping protocol was established, a DNA template for PCR was isolated from ~3 mm tail biopsies by incubation in 75 µl alkaline lysis buffer (25 mM NaOH, 0.2 mM disodium EDTA, pH = 12) for 30 min at 95°C. This was followed by 75 µl neutralization solution (40 mM Tris-HCl) for 10 min at 4°C. 2 µl of the solution was used as DNA template, and PCR with SigmaRED PCR ReadyMix (Sigma, Catalog # R4775) was performed. The PCR products were loaded on a 2% agarose gel, separated by electrophoresis in 1XTAE buffer, and visualized with SYBR Safe DNA gel stain (Sigma, Catalog # S33102). Primers used for genotyping human PFN1 transgenic mice were: hPFN1 forward: GTTATGAAATGGCCTCCACCT, mPrp reverse: TCAGTGCCAGGGGTATTAGC. A unique product length of 190-bp was generated from the hPFN1 cDNA transgene. mPrp forward: GAGCAGGCCATGATCCATT, mPrp reverse: TCAGTGCCAGGGGTATTAGC. The product length of 506-bp was generated from mouse endogenous gene.

Motor performance assessment by rotarod apparatus

Motor performance was assessed using a rotarod apparatus (Harvard Panlab Rota-Rod apparatus, Holliston, MA), as described elsewhere (64). Briefly, motor performance was measured via the latency to fall from a rod rotating at a constant speed of 12 rotations per minute (rpm). A perfect score of 180 s without falling was the benchmark used to track performance. Each mouse participated in three trials per test session (max 3 min), with the best result of three trials recorded.

Gait analysis

Mouse gait parameters were assessed using Noldus CATWALK as well as by manual application of non-toxic ink to paws. The imprints of ink paws on paper were used to assess gait abnormality and stride lengths.

Weight

Animal weights were recorded twice a week starting at P50.

Western blotting

Fresh or snap-frozen tissues were homogenized with RIPA buffer, mixed with sample loading buffer (6% SDS, 15% 2-mercaptoethanol, 30% glycerol, and 0.3 mg/ml bromophenol blue in 188 mM Tris-HCl, pH 6.8), heated at 90°C for 10 min, and separated by 4–12% Bis-Tris Gel (Invitrogen). Separated proteins in the gels were transferred onto nitrocellulose membrane at 380 mA for 45 min (30). The blotted membrane was blocked with 5% skim milk in TBS containing 0.05% Tween 20 (TBS-T buffer) for 30–60 min. After washing the membrane with TBS-T primary antibodies,

including profilin1 (Sigma Catalog # P7749), ubiquitin (Millipore Catalog # MAB1510), and GAPDH (Cell Signaling Catalog# 14C10), it was diluted in TBS-T, 5% milk was added, and the membrane was incubated overnight at 4 °C. The bound antibodies were detected by horseradish peroxidase-conjugated secondary antibody (Amersham Corp.) followed by the ECL detection system (Amersham), according to the manufacturer's instruction.

Soluble and insoluble fractionation

Freshly isolated or frozen spinal cords were processed for fractionation, as described in Wu et al., 2012 with some modifications. Isolated tissues were homogenized in NP-40 lysis buffer containing (1% NP-40, 20mM TrisHCl pH. 7.4, 150mM NaCl, 5mM EDTA, 10% glycerol, 1mM DTT, 10mM sodium fluoride, 1mM sodium orthovanadate, 5mM sodium pyrophosphate) with EDTA-free protease inhibitors (Complete, Roche). The lysates were rotated for 30 min at 4 °C, followed by centrifugation at 13,500rpm for 20 min. The supernatant was removed and used as the soluble fraction. To remove carryovers, the pellet was washed with lysis buffer and resuspended in urea-SDS buffer (NP-40 Lysis Buffer with 8 M urea/3% SDS) followed by sonication. The lysate was then spun again for 20 min at 4 °C and the supernatant was removed (insoluble fraction). Protein concentrations were determined by the BCA assay.

Perfusion

Mice were deeply anaesthetized with isoflurane, followed by transcardial perfusion with 4% paraformaldehyde for immunohistochemistry or 4% paraformaldehyde and 2.5% glutaraldehyde for electron microscopy. Brain, spinal cord, and gastrocnemius muscle were removed and post-fixed overnight in 4% paraformaldehyde or 4% paraformaldehyde and 2.5% glutaraldehyde, as previously described (64).

Immunohistochemistry

Paraffin-embedded sections

Brains were sectioned coronally (50 µm thick) using a vibratome (Leica) and collected in 12-well plates. Immunocytochemistry was performed on every 12th tissue section. Sections were mounted onto glass slides and dried overnight at ambient temperature. They were then deparaffinized with xylene, hydrated in descending concentrations of ethanol, rinsed in water, and immersed in 0.5% cresyl violet for 3 hours. After dehydration in ascending ethanol and xylene, the slides were cover slipped with DEPEX Mounting Media (Electron Microscopy Sciences). Sections were incubated with 0.01 M sodium citrate, pH 9.0 in an 80 °C water bath for 3 hours for antigen retrieval followed by blocking (PBS, 0.05% BSA, 2% FBS, 1% Triton X-100, and 0.1% saponin). Primary antibodies for profilin1 (1:1000, Sigma), anti-Map2 (1:500; Millipore), anti-Ctip2 (1:500; Abcam), and anti-Cry-mu (1:200; Atlas Antibodies) were applied and incubated overnight at 4 °C. Secondary antibodies (i.e., 1:500, Alexa-Fluor 488 or 647; Invitrogen) were applied in blocking solution for 2 hours at room temperature in the dark. Sections were mounted and cover slipped with Fluoromount (Electron Microscopy Sciences). Quantification of pixel (DAB induced brown colour) was analysed by ImageJ.

Frozen sections

Tissues were cryopreserved by incubation in 20% sucrose until tissue sank (1–2 days), frozen in the TissueTek cutting medium

(Sakura Finetek, Torrance, CA). The spinal cords were cut into longitudinal sections 30 µm in thickness with cryostat (Leica CM1900). Unspecific binding sites were blocked by incubation with (PBS, 5% FBS, 0.5% Triton X-100) for 2 hours at room temperature. Primary and secondary antibodies were suspended in (PBS, 1% FBS, 0.1% Triton X-100). Sections were incubated overnight at 4 °C with primary antibodies: profilin1 (1:1000, Sigma), GFAP (1:1000; Novus Biologicals NB-300-141), and IBA1 (1:1000; Wako 019-19741) and 2 hours at room temperature with secondary antibodies (i.e., 1:500, Alexa-Fluor 488 or 647; Invitrogen). F/G-actin ratio was assayed by staining tissues with phalloidin (1:200, Sigma) to detect F-actin and DNaseI conjugates (1:200, ThermoFisher) to detect G-actin. Sections were mounted onto glass slides with DAPI/anti-fade mounting medium (Vector Laboratories). Images were taken with Zeiss Confocal Microscope Confocal LSM 510 (Zeiss, Thornwood, NY). Quantification of fluorescence intensity was analysed by ImageJ.

Neuromuscular junction immunohistochemistry

Gastrocnemius muscle was dissected from mice, fixed with 4% paraformaldehyde, and processed as described in (16).

Electron microscopy

Spinal cord ventral roots were dissected and fixed overnight at 4 °C in 2.5% glutaraldehyde (Electron Microscopy Sciences)/0.05% malachite green (Sigma) in 0.1M sodium cacodylate buffer, pH 7.2 (EMS). After washing with 0.1M sodium cacodylate buffer, the samples were postfixed for 2 hours with 1% osmium tetroxide (EMS)/0.8% potassium hexaferrocyanide (Sigma) for 2 hours and 1% tannic acid (EMS) for 20 min. The samples were rinsed with molecular grade water, stained with 0.5% uranyl acetate (EMS) for 1 hour, and then dehydrated with a graded alcohol series and propylene oxide before embedding in Araldite/Embed 812 (EMS). Thin sections were cut on a Leica UC7 ultramicrotome, collected on formvar carbon coated slot grids, and post stained with uranyl acetate and lead citrate. Imaging was taken with a Technai F20 (FEI) at 80kv.

Measurement of CMAP amplitude

With the mouse under 2% isoflurane anaesthesia, the sciatic nerve was stimulated percutaneously by single pulses of 0.1 ms duration (VikingQuest NCS/EMG Portable EMG machine) delivered through a pair of needle electrodes placed at the sciatic notch. CMAP was recorded with the recording electrode placed sub-dermally on the muscle belly of the TA muscle. A reference electrode was placed near the ankle and a ground electrode at the animals' back, near the midline. Disposable mono-polar needle electrodes (25mm, 28G; catalog # 902-DMF25-TP, Natus Medical Inc., San Carlos, CA) were used for both stimulating and recording. The CMAP trace used for analysis from a given animal/leg was obtained from 4 supra-maximal stimuli. The CMAP value of an individual animal at a given time point represents the averaged peak-to-peak amplitude of both left and right legs. CMAP plot represents average CMAP of all animals ± SEM. Data were analysed with unpaired t-tests.

Stereological cell counts

Nissl positive neurons were counted using standard procedures for stereological analysis, as performed routinely in our laboratory and described elsewhere (65).

Imaging and quantification of CSMN

Sections were analysed using an Eclipse TE2000-E microscope (Nikon). Epifluorescence images were acquired with a Digital Sight DS-Qi1MC CCD camera (Nikon), and light images were acquired with Digital Sight DS-Fi1 camera (Nikon). Quantitative analyses were performed on 3 matched sections (Section 1: Bregma 1.18 mm, interaural 4.98 mm; Section 2: Bregma 0.74 mm, interaural 4.54 mm; Section 3: Bregma 0.14 mm, interaural 3.94 mm) that spanned the motor cortex from hPFN1^{G118V} mice (at the onset of ALS, $n=3$; end-stage disease $n=6$) and age-matched wild type mice (non-TG), ($n=3$; end-stage disease $n=6$). An equivalent area of the motor cortex in three serial sections (at least ~ 600 μm apart) was imaged with 10X objective field per mouse that represents the motor cortex area. The total numbers of large-diameter, Ctip2⁺ neurons in layer V of the motor cortex were blindly counted in a total of three sections per mouse.

Nissl staining

Sections were stained with 0.75% cresyl violet, dehydrated through graded alcohols (70, 95, 100% 2 \times), placed in xylene and cover slipped using DPX mountant.

H&E staining

H&E staining was performed on 5 μm paraffin sections using standard H&E staining protocol.

Statistical analyses

All statistical analyses were performed using Prism software (version 5; Graphpad Software Inc., La Jolla, CA). D'Agostino and Pearson Normality tests were performed on all data prior to analysis. Statistical differences between non-TG, hPFN1^{WT} and hPFN1^{G118V} mice were determined using a one-way ANOVA with post hoc Tukey's multiple comparison tests using GraphPad. Repeated measure ANOVA was used for weight and Rotarod data. Kaplan-Meier analysis was used for survival data. Data were considered statistically significant at $P < 0.05$.

Supplementary Material

Supplementary Material is available at HMG online.

Acknowledgements

The authors are grateful to Dr. Nancy Rusch for valuable discussions and comments on the manuscript. Dr. Paymaan Jafar-Nejad is acknowledged for his helpful and constructive discussion. We acknowledge the valuable help of medical student, Garrett Waggoner, and summer students, Ezra Feldman, Ferhan Kawser and Gabriel Munson.

Conflict of Interest statement. F.R., and K.K.Y.L., are paid employees of Ionis Pharmaceuticals. None declared for other authors.

Funding

This work was supported by the following funding agencies. The authors acknowledge funding for support of this study by grants from the University of Arkansas for Medical Sciences Startup Fund, Pepper Center Pilot Award, University of Arkansas for Medical Sciences Center for Translational Neurosciences, National Institute of General Medical Sciences

IDEA Program Award P30 GM110702, P20GM109005, VA Merit Review I01 BX002425-01.

M.K., gratefully acknowledges the grant support by the National Institute of Neurological Disorders and Stroke, NS088653. The University of Arkansas for Medical Sciences college of Medicine Pilot Study grant award partially supported this study. M.M. is supported by NIH/NICHHD Grant R01HD087057.

Work by P.H.O.'s laboratory was supported by the National Institute of Neurological Disorders and Stroke NS085750 and a grant from the Les Turner ALS Foundation.

R.H.B. gratefully acknowledges the ALS Association, the ALS/FTD ALS Genetics Consortium, the National Institutes of Health/National Institute of Neurological Disorders and Stroke (R01NS088689, R01FD004127, R01NS079836, R01NS065847, R01NS073873), the ALS Therapy Alliance, the Angel Fund, and Project ALS.

O.P. is supported by the Michael J. Fox Foundation. Funds to pay for Open Access publication charges were provided by the UAMS Department of Pharmacology and Toxicology, and by the UAMS College of Medicine Start-up Account to Dr. Kiaei.

References

1. Sreedharan, J. and Brown, R.H. Jr. (2013) Amyotrophic lateral sclerosis: Problems and prospects. *Ann. Neurol.*, **74**, 309–316.
2. Kiernan, M.C., Vucic, S., Cheah, B.C., Turner, M.R., Eisen, A., Hardiman, O., Burrell, J.R. and Zoing, M.C. (2011) Amyotrophic lateral sclerosis. *Lancet*, **377**, 942–955.
3. Rosen, D.R. (1993) Mutations in Cu/Zn superoxide dismutase gene are associated with familial amyotrophic lateral sclerosis. *Nature*, **364**, 362.
4. Renton, A.E., Chio, A. and Traynor, B.J. (2014) State of play in amyotrophic lateral sclerosis genetics. *Nat. Neurosci.*, **17**, 17–23.
5. van Blitterswijk, M., DeJesus-Hernandez, M. and Rademakers, R. (2012) How do C9ORF72 repeat expansions cause amyotrophic lateral sclerosis and frontotemporal dementia: can we learn from other noncoding repeat expansion disorders?. *Curr. Opin. Neurol.*, **25**, 689–700.
6. Jiao, B., Tang, B., Liu, X., Yan, X., Zhou, L., Yang, Y., Wang, J., Xia, K. and Shen, L. (2014) Identification of C9orf72 repeat expansions in patients with amyotrophic lateral sclerosis and frontotemporal dementia in mainland China. *Neurobiol. Aging*, **35**, 936 e919–922.
7. Abramzon, Y., Johnson, J.O., Scholz, S.W., Taylor, J.P., Brunetti, M., Calvo, A., Mandrioli, J., Benatar, M., Mora, G., Restagno, G., et al. (2012) Valosin-containing protein (VCP) mutations in sporadic amyotrophic lateral sclerosis. *Neurobiol. Aging*, **33**, 2231 e2231–2231 e2236.
8. Mackenzie, I.R., Rademakers, R. and Neumann, M. (2010) TDP-43 and FUS in amyotrophic lateral sclerosis and frontotemporal dementia. *Lancet Neurol.*, **9**, 995–1007.
9. Iida, A., Hosono, N., Sano, M., Kamei, T., Oshima, S., Tokuda, T., Nakajima, M., Kubo, M., Nakamura, Y. and Ikegawa, S. (2012) Novel deletion mutations of OPTN in amyotrophic lateral sclerosis in Japanese. *Neurobiol. Aging*, **33**, 1843 e1819–1824.
10. Smith, B.N., Ticozzi, N., Fallini, C., Gkazi, A.S., Topp, S., Kenna, K.P., Scotter, E.L., Kost, J., Keagle, P., Miller, J.W., et al. (2014) Exome-wide Rare Variant Analysis Identifies TUBA4A Mutations Associated with Familial ALS. *Neuron*, **84**, 324–331.
11. Gurney, M.E., Pu, H., Chiu, A.Y., Dal Canto, M.C., Polchow, C.Y., Alexander, D.D., Caliendo, J., Hentati, A., Kwon, Y.W., Deng, H.X., et al. (1994) Motor neuron degeneration in mice that express a human Cu, Zn superoxide dismutase mutation. *Science*, **264**, 1772–1775.

12. Bruijn, L.I., Becher, M.W., Lee, M.K., Anderson, K.L., Jenkins, N.A., Copeland, N.G., Sisodia, S.S., Rothstein, J.D., Borchelt, D.R., Price, D.L., et al. (1997) ALS-linked SOD1 mutant G85R mediates damage to astrocytes and promotes rapidly progressive disease with SOD1-containing inclusions. *Neuron*, **18**, 327–338.
13. Ripps, M.E., Huntley, G.W., Hof, P.R., Morrison, J.H. and Gordon, J.W. (1995) Transgenic mice expressing an altered murine superoxide dismutase gene provide an animal model of amyotrophic lateral sclerosis. *Proc. Natl. Acad. Sci. U. S. A.*, **92**, 689–693.
14. Wong, P.C., Pardo, C.A., Borchelt, D.R., Lee, M.K., Copeland, N.G., Jenkins, N.A., Sisodia, S.S., Cleveland, D.W. and Price, D.L. (1995) An adverse property of a familial ALS-linked SOD1 mutation causes motor neuron disease characterized by vacuolar degeneration of mitochondria. *Neuron*, **14**, 1105–1116.
15. Wegorzewska, I., Bell, S., Cairns, N.J., Miller, T.M. and Baloh, R.H. (2009) TDP-43 mutant transgenic mice develop features of ALS and frontotemporal lobar degeneration. *Proc. Natl. Acad. Sci. U.S.A.*, **106**, 18809–18814.
16. Peters, O.M., Cabrera, G.T., Tran, H., Gendron, T.F., McKeon, J.E., Metterville, J., Weiss, A., Wightman, N., Salameh, J., Kim, J., et al. (2015) Human C9orf72 Hexanucleotide Expansion Reproduces RNA Foci and Dipeptide Repeat Proteins but Not Neurodegeneration in BAC Transgenic Mice. *Neuron*, **88**, 902–909.
17. Liu, Y., Pattamatta, A., Zu, T., Reid, T., Bardhi, O., Borchelt, D.R., Yachnis, A.T. and Ranum, L.P. (2016) C9orf72 BAC Mouse Model with Motor Deficits and Neurodegenerative Features of ALS/FTD. *Neuron*, **90**, 521–534.
18. Mitchell, J.C., McGoldrick, P., Vance, C., Hortobagyi, T., Sreedharan, J., Rogelj, B., Tudor, E.L., Smith, B.N., Klasen, C., Miller, C.C., et al. (2013) Overexpression of human wild-type FUS causes progressive motor neuron degeneration in an age- and dose-dependent fashion. *Acta Neuropathol.*, **125**, 273–288.
19. Huang, C., Zhou, H., Tong, J., Chen, H., Liu, Y.J., Wang, D., Wei, X. and Xia, X.G. (2011) FUS transgenic rats develop the phenotypes of amyotrophic lateral sclerosis and frontotemporal lobar degeneration. *PLoS Genet.*, **7**, e1002011.
20. Ingre, C., Landers, J.E., Rizik, N., Volk, A.E., Akimoto, C., Birve, A., Hubers, A., Keagle, P.J., Piotrowska, K., Press, R., et al. (2013) A novel phosphorylation site mutation in profilin 1 revealed in a large screen of US, Nordic, and German amyotrophic lateral sclerosis/frontotemporal dementia cohorts. *Neurobiol Aging*, **34**, 1708 e1701–1706.
21. Smith, B.N., Vance, C., Scotter, E.L., Troakes, C., Wong, C.H., Topp, S., Maekawa, S., King, A., Mitchell, J.C., Lund, K., et al. (2015) Novel mutations support a role for Profilin 1 in the pathogenesis of ALS. *Neurobiol Aging*, **36**, 1602 e1617–1627.
22. Wu, C.H., Fallini, C., Ticozzi, N., Keagle, P.J., Sapp, P.C., Piotrowska, K., Lowe, P., Koppers, M., McKenna-Yasek, D., Baron, D.M., et al. (2012) Mutations in the profilin 1 gene cause familial amyotrophic lateral sclerosis. *Nature*, **488**, 499–503.
23. Chen, Y., Zheng, Z.Z., Huang, R., Chen, K., Song, W., Zhao, B., Chen, X., Yang, Y., Yuan, L. and Shang, H.F. (2013) PFN1 mutations are rare in Han Chinese populations with amyotrophic lateral sclerosis. *Neurobiol Aging*, **34**, 1922 e1921–1925.
24. Witke, W., Podtelejnikov, A.V., Di Nardo, A., Sutherland, J.D., Gurniak, C.B., Dotti, C. and Mann, M. (1998) In mouse brain profilin I and profilin II associate with regulators of the endocytic pathway and actin assembly. *Embo J.*, **17**, 967–976.
25. Pantaloni, D. and Carlier, M.F. (1993) How profilin promotes actin filament assembly in the presence of thymosin beta 4. *Cell*, **75**, 1007–1014.
26. Kang, F., Purich, D.L. and Southwick, F.S. (1999) Profilin promotes barbed-end actin filament assembly without lowering the critical concentration. *J. Biol. Chem.*, **274**, 36963–36972.
27. Wolven, A.K., Belmont, L.D., Mahoney, N.M., Almo, S.C. and Drubin, D.G. (2000) In vivo importance of actin nucleotide exchange catalyzed by profilin. *J. Cell Biol.*, **150**, 895–904.
28. Witke, W. (2004) The role of profilin complexes in cell motility and other cellular processes. *Trends Cell Biol.*, **14**, 461–469.
29. Haarer, B.K., Petzold, A.S. and Brown, S.S. (1993) Mutational analysis of yeast profilin. *Mol. Cell Biol.*, **13**, 7864–7873.
30. Lu, P.J., Shieh, W.R., Rhee, S.G., Yin, H.L. and Chen, C.S. (1996) Lipid products of phosphoinositide 3-kinase bind human profilin with high affinity. *Biochemistry*, **35**, 14027–14034.
31. Moens, P.D. and Bagatolli, L.A. (2007) Profilin binding to sub-micellar concentrations of phosphatidylinositol (4,5) bisphosphate and phosphatidylinositol (3,4,5) trisphosphate. *Biochim. Biophys. Acta*, **1768**, 439–449.
32. Tang, Z., Araysi, L.M. and Fathallah-Shaykh, H.M. (2013) c-Src and neural Wiskott-Aldrich syndrome protein (N-WASP) promote low oxygen-induced accelerated brain invasion by gliomas. *PLoS One*, **8**, e75436.
33. Serrano-Pertierra, E., Cernuda-Morollon, E. and Lopez-Larrea, C. (2012) Wiskott-Aldrich syndrome protein (WASp) and N-WASp are involved in the regulation of NK-cell migration upon NKG2D activation. *Eur. J. Immunol.*, **42**, 2142–2151.
34. Boopathy, S., Silvas, T.V., Tischbein, M., Jansen, S., Shandilya, S.M., Zitzewitz, J.A., Landers, J.E., Goode, B.L., Schiffer, C.A. and Bosco, D.A. (2015) Structural basis for mutation-induced destabilization of profilin 1 in ALS. *Proc. Natl. Acad. Sci. U. S. A.*, **112**, 7984–7989.
35. Ross, C.A., Wood, J.D., Schilling, G., Peters, M.F., Nucifora, F.C., Jr., Cooper, J.K., Sharp, A.H., Margolis, R.L. and Borchelt, D.R. (1999) Polyglutamine pathogenesis. *Philos. Trans. R. Soc. Lond. B Biol. Sci.*, **354**, 1005–1011.
36. Xu, Y.F., Zhang, Y.J., Lin, W.L., Cao, X., Stetler, C., Dickson, D.W., Lewis, J. and Petrucelli, L. (2011) Expression of mutant TDP-43 induces neuronal dysfunction in transgenic mice. *Mol. Neurodegener.*, **6**, 73.
37. Goodman, B.P., Harper, C.M. and Boon, A.J. (2009) Prolonged compound muscle action potential duration in critical illness myopathy. *Muscle Nerve*, **40**, 1040–1042.
38. Tanaka, Y., Nonaka, T., Suzuki, G., Kametani, F. and Hasegawa, M. (2016) Gain-of-function profilin 1 mutations linked to familial amyotrophic lateral sclerosis cause seed-dependent intracellular TDP-43 aggregation. *Hum. Mol. Genet.*, **25**, 1420–1433.
39. Conforti, L., Gilley, J. and Coleman, M.P. (2014) Wallerian degeneration: an emerging axon death pathway linking injury and disease. *Nat. Rev. Neurosci.*, **15**, 394–409.
40. Jara, J.H., Genc, B., Cox, G.A., Bohn, M.C., Roos, R.P., Macklis, J.D., Ulupinar, E. and Ozdinler, P.H. (2015) Corticospinal Motor Neurons Are Susceptible to Increased ER Stress and Display Profound Degeneration in the Absence of UCHL1 Function. *Cereb. Cortex*, **25**, 4259–4272.
41. Gautam, M., Jara, J.H., Sekerkova, G., Yasvoina, M.V., Martina, M. and Ozdinler, P.H. (2016) Absence of alsin function leads to corticospinal motor neuron vulnerability via novel disease mechanisms. *Hum. Mol. Genet.*, **25**, 1074–1087.

42. Jara, J.H., Villa, S.R., Khan, N.A., Bohn, M.C. and Ozdinler, P.H. (2012) AAV2 mediated retrograde transduction of corticospinal motor neurons reveals initial and selective apical dendrite degeneration in ALS. *Neurobiol. Dis.*, **47**, 174–183.
43. Lambrechts, A., Jonckheere, V., Dewitte, D., Vandekerckhove, J. and Ampe, C. (2002) Mutational analysis of human profilin I reveals a second PI(4,5)-P2 binding site neighbouring the poly(L-proline) binding site. *BMC Biochem.*, **3**, 12.
44. Cotta-de-Almeida, V., Westerberg, L., Maillard, M.H., Onaldi, D., Wachtel, H., Meelu, P., Chung, U.I., Xavier, R., Alt, F.W. and Snapper, S.B. (2007) Wiskott Aldrich syndrome protein (WASP) and N-WASP are critical for T cell development. *Proc. Natl Acad. Sci. U S A*, **104**, 15424–15429.
45. Lutskiy, M.I., Park, J.Y., Remold, S.K. and Remold-O'Donnell, E. (2008) Evolution of highly polymorphic T cell populations in siblings with the Wiskott-Aldrich Syndrome. *PLoS One*, **3**, e3444.
46. Park, H. and Cox, D. (2009) Cdc42 regulates Fc gamma receptor-mediated phagocytosis through the activation and phosphorylation of Wiskott-Aldrich syndrome protein (WASP) and neural-WASP. *Mol. Biol. Cell*, **20**, 4500–4508.
47. Saggi, S.K., Chotaliya, H.P., Blumbergs, P.C. and Casson, R.J. (2010) Wallerian-like axonal degeneration in the optic nerve after excitotoxic retinal insult: an ultrastructural study. *BMC Neurosci.*, **11**, 97.
48. Gilley, J. and Coleman, M.P. (2010) Endogenous Nmnat2 is an essential survival factor for maintenance of healthy axons. *PLoS Biol.*, **8**, e1000300.
49. Moloney, E.B., de Winter, F. and Verhaagen, J. (2014) ALS as a distal axonopathy: molecular mechanisms affecting neuromuscular junction stability in the presymptomatic stages of the disease. *Front Neurosci.*, **8**, 252.
50. Brettle, M., Suchowerska, A.K., Chua, S.W., Ittner, L.M. and Fath, T. (2015) Amyotrophic lateral sclerosis-associated mutant profilin 1 increases dendritic arborisation and spine formation in primary hippocampal neurons. *Neurosci. Lett.*, **609**, 223–228.
51. Freischmidt, A., Schopflin, M., Feiler, M.S., Fleck, A.K., Ludolph, A.C. and Weishaupt, J.H. (2015) Profilin 1 with the amyotrophic lateral sclerosis associated mutation T109M displays unaltered actin binding and does not affect the actin cytoskeleton. *BMC Neurosci.*, **16**, 77.
52. Alkam, D., Feldman, E.Z., Singh, A. and Kiaei, M. (2016) Profilin1 biology and its mutation, actin(g) in disease. *Cell. Mol. Life Sci.*, **74**, 1–15.
53. Rust, M.B., Kullmann, J.A. and Witke, W. (2012) Role of the actin-binding protein profilin1 in radial migration and glial cell adhesion of granule neurons in the cerebellum. *Cell Adh. Migr.*, **6**, 13–17.
54. Birbach, A. (2008) Profilin, a multi-modal regulator of neuronal plasticity. *Bioessays*, **30**, 994–1002.
55. Nolle, A., Zeug, A., van Bergeijk, J., Tonges, L., Gerhard, R., Brinkmann, H., Al Rayes, S., Hensel, N., Schill, Y., Apkhazava, D., et al. (2011) The spinal muscular atrophy disease protein SMN is linked to the Rho-kinase pathway via profilin. *Hum. Mol. Genet.*, **20**, 4865–4878.
56. Del Poggetto, E., Bemporad, F., Tatini, F. and Chiti, F. (2015) Mutations of Profilin-1 Associated with Amyotrophic Lateral Sclerosis Promote Aggregation Due to Structural Changes of Its Native State. *ACS Chem. Biol.*, **10**, 2553–2563.
57. Del Poggetto, E., Chiti, F. and Bemporad, F. (2015) The Folding process of Human Profilin-1, a novel protein associated with familial amyotrophic lateral sclerosis. *Sci. Rep.*, **5**, 12332.
58. Del Poggetto, E., Gori, L. and Chiti, F. (2016) Biophysical analysis of three novel profilin-1 variants associated with amyotrophic lateral sclerosis indicates a correlation between their aggregation propensity and the structural features of their globular state. *Biol. Chem.*, **397**, 927–937.
59. Arai, T., Hasegawa, M., Akiyama, H., Ikeda, K., Nonaka, T., Mori, H., Mann, D., Tsuchiya, K., Yoshida, M., Hashizume, Y., et al. (2006) TDP-43 is a component of ubiquitin-positive tau-negative inclusions in frontotemporal lobar degeneration and amyotrophic lateral sclerosis. *Biochem. Biophys. Res. Commun.*, **351**, 602–611.
60. Neumann, M., Sampathu, D.M., Kwong, L.K., Truax, A.C., Micsenyi, M.C., Chou, T.T., Bruce, J., Schuck, T., Grossman, M., Clark, C.M., et al. (2006) Ubiquitinated TDP-43 in frontotemporal lobar degeneration and amyotrophic lateral sclerosis. *Science*, **314**, 130–133.
61. Yang, C., Danielson, E.W., Qiao, T., Metterville, J., Brown, R.H., Jr., Landers, J.E. and Xu, Z. (2016) Mutant PFN1 causes ALS phenotypes and progressive motor neuron degeneration in mice by a gain of toxicity. *Proc. Natl. Acad. Sci. U. S. A.*, **113**, E6209–E6218.
62. Fischer, M., Rulicke, T., Raeber, A., Sailer, A., Moser, M., Oesch, B., Brandner, S., Aguzzi, A. and Weissmann, C. (1996) Prion protein (PrP) with amino-proximal deletions restoring susceptibility of PrP knockout mice to scrapie. *Embo J.*, **15**, 1255–1264.
63. Schilling, G., Becher, M.W., Sharp, A.H., Jinnah, H.A., Duan, K., Kotzok, J.A., Slunt, H.H., Ratovitski, T., Cooper, J.K., Jenkins, N.A., et al. (1999) Intranuclear inclusions and neuritic aggregates in transgenic mice expressing a mutant N-terminal fragment of huntingtin. *Hum. Mol. Genet.*, **8**, 397–407.
64. Esmaeili, M.A., Yadav, S., Gupta, R.K., Waggoner, G.R., Deloach, A., Calingasan, N.Y., Beal, M.F. and Kiaei, M. (2016) Preferential PPAR-alpha activation reduces neuroinflammation, and blocks neurodegeneration in vivo. *Hum. Mol. Genet.*, **25**, 317–327.
65. Kiaei, M., Petri, S., Kipiani, K., Gardian, G., Choi, D.K., Chen, J., Calingasan, N.Y., Schafer, P., Muller, G.W., Stewart, C., et al. (2006) Thalidomide and lenalidomide extend survival in a transgenic mouse model of amyotrophic lateral sclerosis. *J. Neurosci.*, **26**, 2467–2473.